ALMA MATER STUDIORUM – UNIVERSITY OF BOLOGNA
DEPARTMENT OF ELECTRICAL ENGINEERING

PhD in Electrical Engineering ING-IND/31
XIX Cycle - March 2007

Analysis of the Heatsink Influence on Conducted and Radiated Electromagnetic Interference in Power Electronic Converters

PhD Student: Andrea Dolente

Tutor: Prof. Ugo Reggiani

Coordinator: Prof. Francesco Negrini

CONTENTS

1 Introduction

1.1 Overview....1

1.2 Summary of Contributions....2

1.3 Outline of Thesis....2

2 Literature Review

2.1 Introduction....3

2.2 The Role of Heatsinks in EMI Generation....4

2.3 Modelling Approaches for Heatsinks in Power Electronics....5

2.4 EMI Control....6

References....7

3 Conducted Emissions from Heatsink

3.1 Introduction....9

3.2 Heatsink with Multiple Sources....10

3.2.1 Conducted Emission Measurements....12

3.2.2 Common-Mode Current Measurements....19

3.3 Switching Waveform of Power Electronic Devices....24

3.3.1 Inductance Models....26

3.3.2 Circuit Simulations and Measurements....31

3.3.3 Common-Mode Current Calculation....35

3.4 Summary....38

Appendix....39

References....40

4 Radiated Emissions from Heatsink

4.1 Introduction....42
4.2 Application of Numerical Methods....42
4.3 Modelling of Heatsink Electromagnetic Characteristics....43
4.4 Numerical Simulations....45
4.4.1 Near-Field Radiation....45
4.4.2 Far-Field Radiation....51
4.5 Summary....61
References....62

5 Conclusions and Open Problems

5.1 Conclusions....63
5.2 Open Problems....64

CHAPTER 1

“Introduction”

1.1 Overview

In the last 20 years Switched-Mode Power Supplies (SMPS) have become an important factor in the deterioration of our electromagnetic environment. Within any electrical/electronic system, power supply assumes a fundamental role by providing consistent and repeatable power to its circuit. The increasing integration of power electronic circuit modules together with the continuing growth in power density, switching speed and operating frequency have resulted in a close interaction between electromagnetic, thermal and mechanical considerations and a significant increase in unwanted parasitic effects. The rapid switching capability of modern semiconductor devices (MOSFET, IGBT, etc) results in very fast voltage and current variations which act on structures such as heatsinks generating parasitic currents, voltage transients and radiated emissions. Altough much research has been carried out on the cooling effect of heatsinks, little is known about their electrical effects. In this thesis different heatsink configurations are analyzed in order to investigate the conducted and radiated electromagnetic interferences associated to them. Particularly emphasis will be given to the effects that a subdivision of the heatsink among the different switching devices may have on the common- and differential-mode components of the conducted EMI generated by the SMPS.

In order to design a power electronic system with properly controlled electromagnetic interference the designer typically uses a set of established EMC rules to estimate various electromagnetic parameters. The estimation of electromagnetic parameters is usually based on simplified analytical expressions which are often very crude approximations of the physical situation. This approach is valid for some applications but recent trends in power electronics design optimisation necessitates the use of computer aided design tools for electromagnetic parameter extraction. This thesis explores the use of computational tools and experimental

measurements to model and extract electromagnetic parameters of structures such as heatsinks and printed circuit board interconnections.

1.2 Summary of contributions

The main contributions of this thesis are summarised as follows:

- The effects on Electromagnetic Interference (EMI) generation that a subdivision of the heatsink among the different switching devices are investigated in terms of conducted and radiated emissions.
- A modelling technique for the design of power printed circuit boards (PCBs), that combines SPICE circuit simulation, electromagnetic simulation and analytical formulae, in order to predict accurately the power device switching waveform, is presented.
- The influence of the geometrical characteristics and the position of the heatsink are studied in terms of the electric far-field emission.

1.3 Outline of Thesis

Chapter 1 outlines the problem, describes the work and summarises the contributions of the thesis.

Chapter 2 chronologically reviews the literature and describes the main results that contributed to the results presented in this thesis.

The first part of the chapter 3 focuses on the influence that different heatsink configurations have on the generation of conducted electromagnetic interference (EMI) in switched-mode power supplies. In order to examine the common-mode voltage applied to the heatsink, the second part of the chapter presents an efficient and effective modelling technique for accurate prediction of the switching waveform of typical power converter systems.

Chapter 4 investigates by means of numerical simulations the influence that different heatsink configurations have on the generation of radiated emission in the near and far field.

Chapter 5 concludes this thesis and discusses directions and suggestions for open problems.

CHAPTER 2

"Literature Review"

2.1 Introduction

An important aspect in the design of electromagnetically compatible electrical and/or electronic systems concerns the power supply. Starting from the early 1970s, linear power supplies have been progressively and extensively replaced by switching systems. Because of the use of square waves with steep slopes, and their typical switching frequencies, that range from a few kHz to about 300 kHz, switched-mode power supplies (SMPS) present indeed higher efficiency and reduced dimensions and weight. On the other hand, these advantages are counterbalanced by the generation of electromagnetic interference that appears as narrowband noise signals, at the basic switching frequency and its harmonics [1], [2], as well as broadband noise signals.

Until about ten years ago the open literature on EMI control and reduction techniques in power electronics was primarily focussed on the analysis of MOSFET switching behaviour and on experimental studies that relate switching waveforms and radiated EMI. The evolution of power electronic systems towards higher switching frequencies, faster speeds, higher integration densities and reduced volume have greatly increased the need for integrated electrical analysis that comprises 3-D electromagnetic modelling and electrical circuit analysis. The development of computers with increased speed has meant that numerical techniques are becoming more effective in solving electromagnetic field problems like the study of radiation and antenna patterns of heatsinks and modelling of power PCB interconnections.

The EMI has the form of both conducted and radiated emissions. The former, that are a primary reason of concern in SMPS, can be produced by differential-mode (DM) and common-mode (CM) current and voltage components. In power electronics equipment CM currents which engender conducted emissions originate from parasitic effects. In regard to

radiated emissions, it is known that they can be adequately estimated and predicted if EMI source mechanisms and their relation to the circuit geometry are correctly modelled. However, the sources of both CM and DM radiations in equipment may be of different nature and difficult to define [3], [4].

2.2 The Role of Heatsinks in EMI Generation

In modern high-power equipment the fast operation of devices leads to heat generation due to switching losses. This heat needs to be dissipated through a heatsink to keep the devices within safe operating conditions. On the other hand, the noise coupled from the device to the heatsink may cause it to act as an efficient antenna and radiate the noise at one or more harmonics of the switching frequency. To minimize the total amount of radiated emission, the heatsink must be electrically small in comparison to the wavelength λ of the highest frequency generated by the switching device. If any dimension of the heatsink is between λ and $\lambda/20$, radiated EMI can be expected [5]. According to finite-difference time-domain (FDTD) simulations of the electric far-field radiation from a simplified heatsink, such as a thin rectangular sheet, there are two main dimensions to be excited, giving two fundamental frequencies and subsequent harmonics which can be enhanced or suppressed by changing the position of the excitation. The addition of fins on the heatsink could reduce the resonant frequency but also increase the amplitude of the electric far-field radiation if they run across the width of the sheet rather than the length [6].

Heatsink electromagnetic characteristics have been analysed for Very Large Scale Integrated (VLSI) applications too. Due to increased operating frequencies of micro-electronic circuits into the GHz region components such as heatsinks become efficient radiators of electromagnetic energy. Today the problem of electromagnetic modelling of VLSI heatsink emissions is a standard problem used to evaluate electromagnetic modelling tools [7]. The application of numerical methods to electromagnetic modelling of heatsinks mounted on VLSI circuits are explored in [8..10]. They show that a grounded heatsink may be an effective way to reduce radiated emissions. The electromagnetic characteristic of the heatsink is affected by different grounding positions but not necessarily by increasing the number of grounding points. The location and number of ground point remains an open question for further research [9].

2.3 Modelling Approaches for Heatsinks in Power Electronics

Heatsink applications in power electronic systems differ from heatsinks mounted on VLSI circuits. A typical heatsink arrangement in AC/DC power conversion is shown in Figure 1.

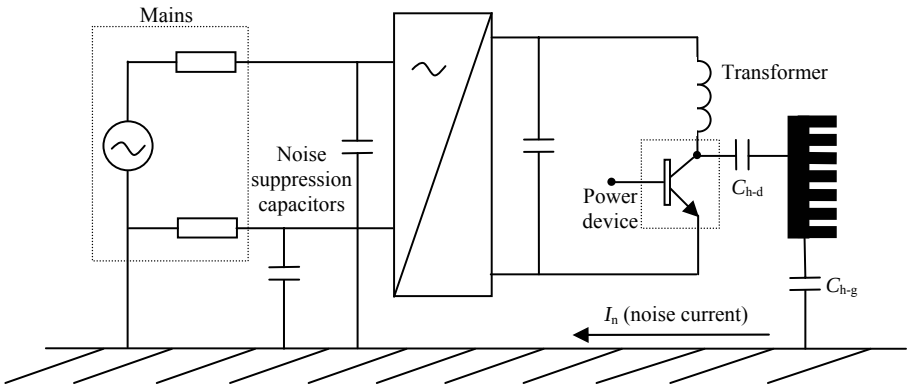

Fig. 1. AC/DC converter with ungrounded heatsink

Since grounding of a heatsink increases conducted EMI in many power electronics applications heatsinks are often not grounded. Heatsinks come in many different geometries and sizes and operate with many different power devices. For thermal and structural reasons an aluminium heatsink is often placed under the whole printed circuit board and the total structure looks like a parallel planes waveguide. The ungrounded heatsink forms capacitive coupling paths to ground. In order to reduce radiation the heatsink can be grounded at the cost of increased common-mode currents to the power supply, escalating conducted EMI, [11]. Common-mode currents can be reduced by increasing the parasitic capacitance between the power device and the heatsink but this may upset the cooling efficiency of the heatsink. Thus, the connection of a heatsink to a power device and the packaging technology is a design issue involving EMI and thermal performance.

The modelling of ungrounded heatsink is based on parasitic mode concepts that are suitable for numerical simulations. The main issues are the implementation of the heatsink problem in a computational space and the selection of the energy sources for the computation of the parasitic capacitance.

2.4 EMI Control

There are many techniques to control EMI in power electronic systems, including reduction of parasitic coupling [12], specialised circuit design (use of resonant converters [13], application of variable frequency switching [14]) and direct control of EMI sources [15], [16]. If such control techniques fail to sufficiently reduce EMI then EMI filters and shielding techniques are often used to further reduce conducted and radiated EMI.

The most effective EMI reduction technique in power electronics design is to directly control the main EMI sources. Unwanted effects including power loss and radiation of fields in the vicinity of the converter can be reduced by controlling the rate of variation of the drain voltage and current in a basic converter cell. This technique is applied and experimentally validated in [15] and [16]. The design method introduced in [15] is based on the control of the drain voltage slope by shaping the gate current in the main power switching devices. The gate charge is controlled by using an additional current source in the gate circuit. The experimental results have shown a reduction in the conducted and radiated emissions of the converter cell. The same EMI reduction technique is used in [16] with the main focus on the analysis of EMI radiational noise from converter systems. It is shown that the radiational noise is generated by the oscillating current flowing through the IGBT's output capacity and the snubber circuit. This circuit, modelled as a high frequency equivalent circuit, produces switching waveforms that can be related to the radiated EMI. The proposed noise reduction method, an active gate drive circuit, reduces voltage rate in the reverse recovery diode and the turn-off overvoltages in the IGBT. The effect of the above circuit on noise reduction was tested on a chopper circuit with an IGBT module by using a measurement system that comprises a dipole antenna and a spectrum analyser. It is shown that the technique is effective in reducing radiational noise. The effectiveness of the technique was also tested by simulation of the radiated EMI noise. The simulation results are based on the oscillating current in an equivalent circuit composed of a snubber capacitor, the output capacitance of the IGBT, wiring inductance and circuit resonance components. The magnitude of the electric far field is calculated from the loop current of the equivalent circuit by far field formulae derived by [17].

Noise reduction techniques [15] and [16] focus on different types of noise such as near magnetic fields and radiated far electric fields.

References

[1] C. R. Paul and K. B. Hardin, "Diagnosis and reduction of conducted noise emission," *IEEE Transactions on Electromagnetic Compatibility*, vol. 30, no. 4, November 1988, pp. 553-560.

[2] M. Mardiguian, *Controlling radiated emissions by design*, 2nd ed., Kluwer Academic Publishers, Boston, USA, 2001.

[3] C. R. Paul and D. R. Bush, "Radiated emissions from common mode currents," in *Proc. IEEE Symposium on Electromagnetic Compatibility*, Atlanta, USA, August 1987, pp. 197–203.

[4] D. M. Hockanson, J. L. Drewniak, T. H. Hubing, T. P. Van Doren, Fei Sha and M. J. Wilhelm, "Investigation of fundamental EMI source mechanisms driving common-mode radiation from printed circuit boards with attached cables," *IEEE Transactions on Electromagnetic Compatibility*, vol. 38, no. 4, November 1996, pp. 557-566.

[5] R. Georgerian and M. I. Montrose, "Product safety and the heat sink-dilemma of minimizing radiated emissions and maximizing thermal cooling," in *Proc. IEEE International Symposium on Electromagnetic Compatibility*, vol. 1, August 18 - 22, 2003, pp. 134-137.

[6] N. J. Ryan, B. Chambers and D. A. Stone, "FDTD modelling of heatsink RF characteristics for EMC mitigation," *IEEE Transactions on Electromagnetic Compatibility*, vol. 44, no. 3, August 2002, pp. 458-465.

[7] B. Archembault, "A proposed set of specific standard EMC problems to help engineers evaluate EMC modelling tools," *IEEE International Symposium on Electromagnetic Compatibility*, vol. 2, August 2001, pp. 1335–1340.

[8] K. Li et al., "Application of FDTD method to analysis of electromagnetic radiation from VLSI heatsink configurations," *IEEE transactions on Electromagnetic Compatibility,* vol. 35, no. 2, May 1993, pp. 204–214.

[9] J. F. Dawson, A. C. Marvin, S. J. Porter, A. Nothofer, J. E. Will and S. Hopkins, "The effect of grounding on radiated emissions from heatsinks," in *Proc. IEEE International Symposium on Electromagnetic Compatibility*, vol. 2, 2001, pp. 1248-1252.

[10] Li Rong and Zhang Lin-Chang, "Heatsink grounding effect on radiated emission of electronic device", in *Proc. 3rd International Symposium on Electromagnetic Compatibility*, May 2002, pp. 704-709.

[11] L. Tihanyi, *Electromagnetic compatibility in power electronics*, J. K. Eckert & Company, Inc., Sarasota, Florida, USA, 1995.

[12] D. Ning and F. C. Lee, "Characterisation and analysis of parasitic parameters and their effects in power electronics circuit", *27th Annual IEEE Transactions on Microwave Theory and Techniques*, vol. 2, June 1996, pp. 1743-1748.

[13] H. Chung, S. Y. R. Hui and K. K. Tse, "Reduction of power converter EMI emission using soft-switching technique," *IEEE transactions on Electromagnetic Compatibility*, vol. 40, no. 3, August 1998.

[14] M. Kuisma, "Variable frequency switching in power supply EMI-control: an overview," *Aerospace and Electronic System Magazine*, IEEE, vol. 18, no.12, December 2003.

[15] A. Consoli, S. Musumeci and G. Oriti, "An innovative EMI reduction design technique in power converters," *IEEE Transactions on Electromagnetic Compatibility*, vol. 38, no. 4, November 1996, pp. 567–575.

[16] S. Igarashi, S. Takizawa, K. Kuroki and T. Shimizu, "Analysis and reduction of radiated EMI noise from converter systems," *Electrical Engineering in Japan*, no. 130 (1), January 2000, pp. 106–117.

[17] J. D. Kraus, *Antennas*, McGraw Hill, 1998.

CHAPTER 3

“Conducted Emissions from Heatsink”

3.1 Introduction

In the first part of the chapter an analysis of the influence that different heatsink configurations have on the generation of conducted electromagnetic interference (EMI) in switched-mode power supplies is provided. A prototype 7 kVA AC/AC voltage regulator with four IGBTs was used for the purpose. A subdivision of its original large heatsink among the switching devices is studied in order to emphasize the effects of the stray capacitance variation on the common-mode component of the EMI. Measurements of conducted emission and of its components were carried out and compared for three heatsink configurations**.** Measurements of common-mode current from a single IGBT are provided as well.

In order to examine the common-mode voltage applied to the heatsink, the second part of the chapter presents an efficient and effective modelling technique for achieving accurate switching waveform for typical power converter systems. The main idea is to combine circuit simulations (SPICE), electromagnetic (EM) simulations and analytical formulae, in order to implement the most suitable method for a power supply circuit topology. The interconnection model of a power printed circuit board (PCB) is based on the high frequency equivalent circuit which relates the interconnection inductance to switching waveform of the power device. The EM simulations based on Finite-Difference Time-Domain (FDTD) and Finite-Element (FE) methods are used to analyse the behaviour of different layouts regarding the parasitic effects. Finally, we propose a fast and efficient simulation technique to limit computation time and to provide both transient and EM analysis for power PCB design.

3.2 Heatsink with Multiple Sources

The effects on conducted EMI generation of a stray capacitance variation for a large heatsink onto which all power semiconductors are mounted, a solution widely adopted in most SMPS in order to provide structural integrity to the converter and sufficient cooling, have been treated in literature [1]. However, not as much emphasis has been given to the effects on conducted EMI generation that a subdivision of the heatsink among the different switching devices may have in SMPS. A prototype 7 kVA AC/AC voltage regulator, based on a PWM technique with a constant switching frequency of 8 kHz, was used for the purpose. In Figure 1 is shown the circuit schematic of the voltage regulator employed in the tests.

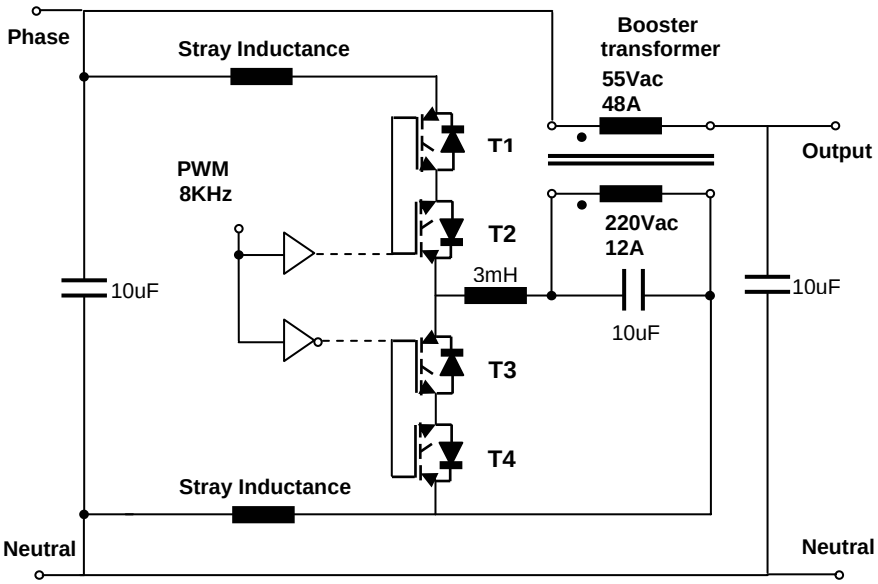

Fig. 1. Voltage regulator circuit

The load voltage is varied by controlling the magnetic flux linking a winding of the transformer. The primary of the transformer is connected in series with the load, while the secondary is shunted with a control device. The flux linkage is controlled by using two switches each consisting in a couple of IGBTs. Three different heatsink configurations, shown with the SMPS voltage regulator in Figure 2, are examined.

Fig. 2. Clockwise from top left: SMPS voltage regulator used in the tests; original single heatsink; two heatsinks; four heatsinks.

The original large heatsink, onto which both IGBT couples are initially mounted, is afterwards subdivided at first in two equal parts, with a switch onto each part, and then in four parts, one for each IGBT. In this last configuration the heatsinks are not reduced to the same dimensions as it is not particularly significant for the purpose of this analysis. The influence of stray capacitances introduced by the different heatsinks is emphasized by means of conducted EMI measurements, that are carried out through two line impedance stabilization networks (LISN, 50Ω/50μH) in order to decouple the AC source from the SMPS. In Figure 3, the high-frequency equivalent circuit of the SMPS, represented as a generic EMI source, and the LISNs is depicted.

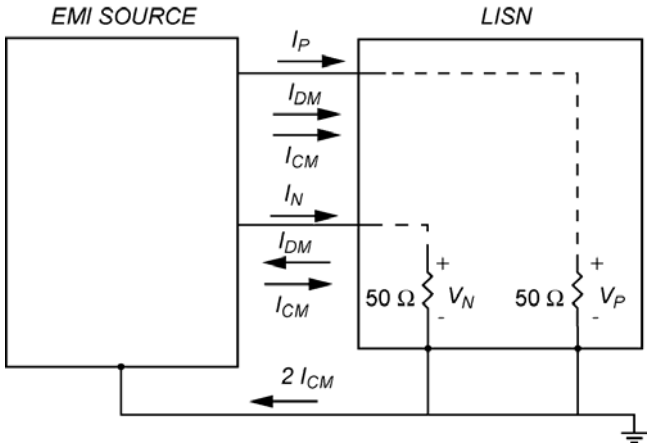

Fig. 3. Equivalent circuit of the LISNs as seen by a typical EMI source in the conducted emission frequency range of use.

In order to separate the common-mode (CM) and differential-mode (DM) conducted emission components, a noise separator that makes use of 0° and 180° power combiners is used [2]. The effects of grounding are also appreciated and highlighted. In the following section a comparison of measurements on the different heatsinks used in the SMPS prototype is carried out and commented on.

3.2.1 Conducted Emission Measurements

In order to carry out EMI measurements, a PMM 7000 EMI receiver (represented by one of the two 50 Ω loads in Figure 3) is connected to the signal terminals of a LISN through a 10 dB attenuator, whereas the signal terminals of the other LISN are terminated with a 50 Ω impedance. In Figures 4-9, the measured quasi-peak spectrum envelopes of the conducted emission and its CM and DM components for the three grounded and ungrounded heatsink configurations of Figure 2 are presented.

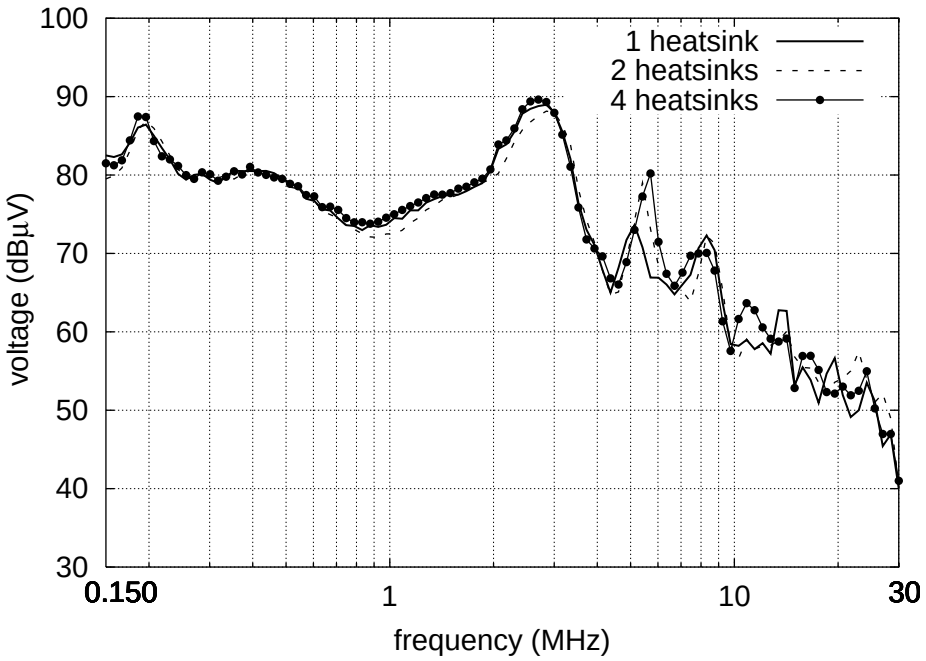

Fig. 4. SMPS conducted emission spectrum for grounded heatsinks.

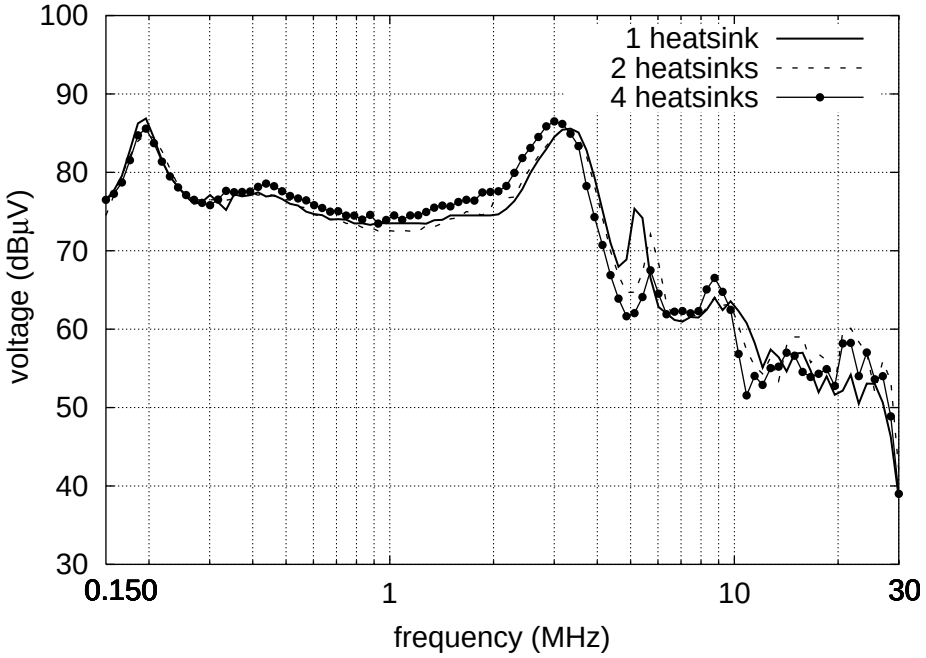

Fig. 5. SMPS conducted emission spectrum for ungrounded heatsinks.

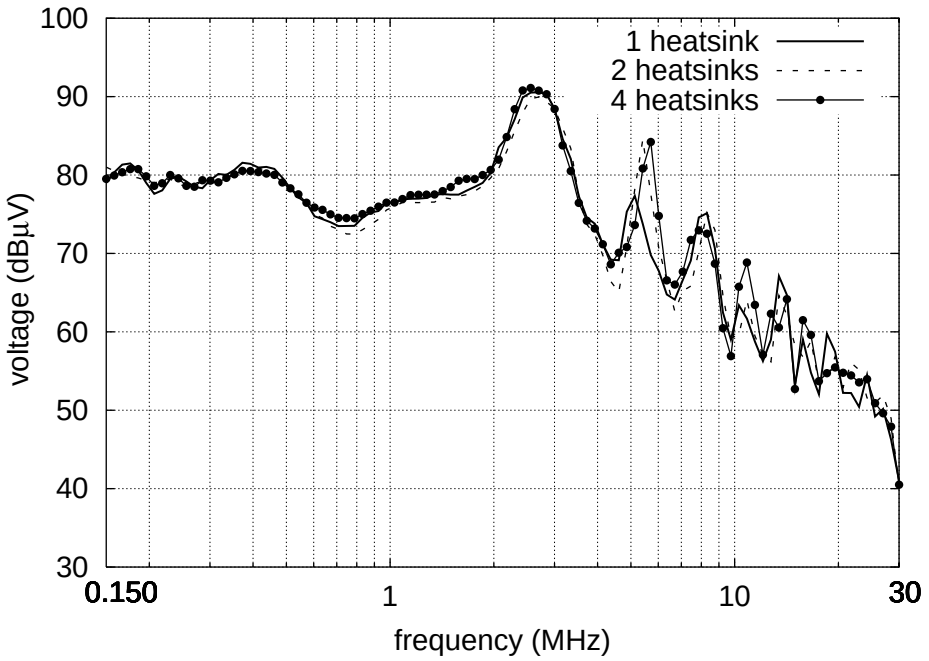

Fig. 6. CM conducted emission spectrum for grounded heatsinks.

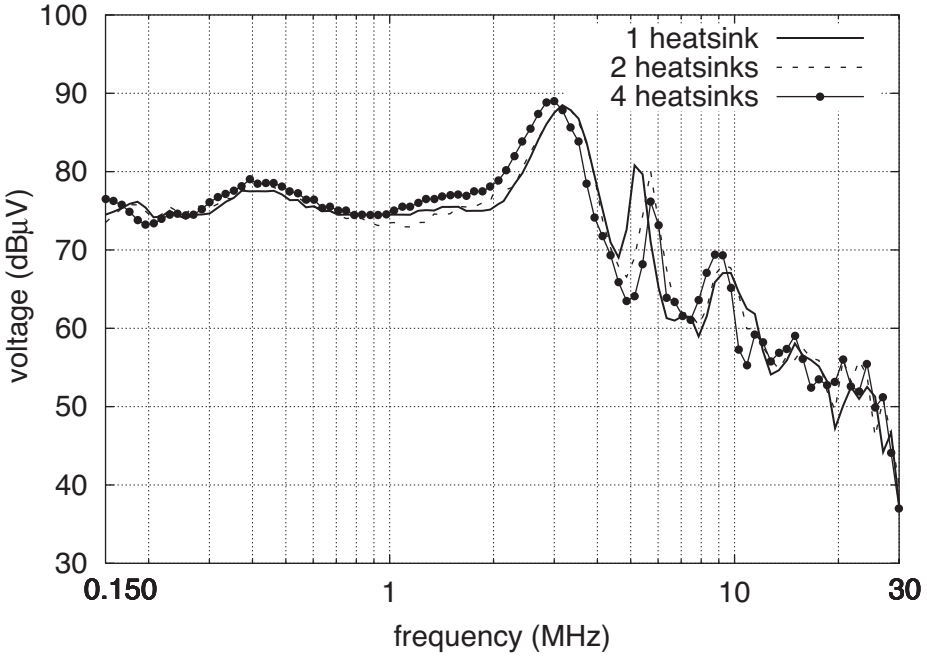

Fig. 7. CM conducted emission spectrum for ungrounded heatsinks.

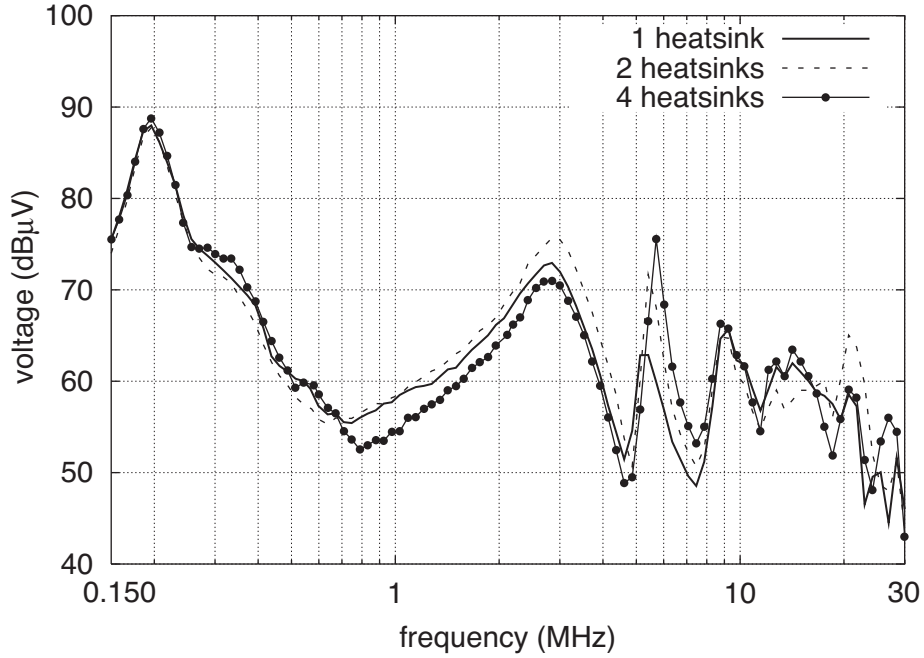

Fig. 8. DM conducted emission spectrum for grounded heatsinks.

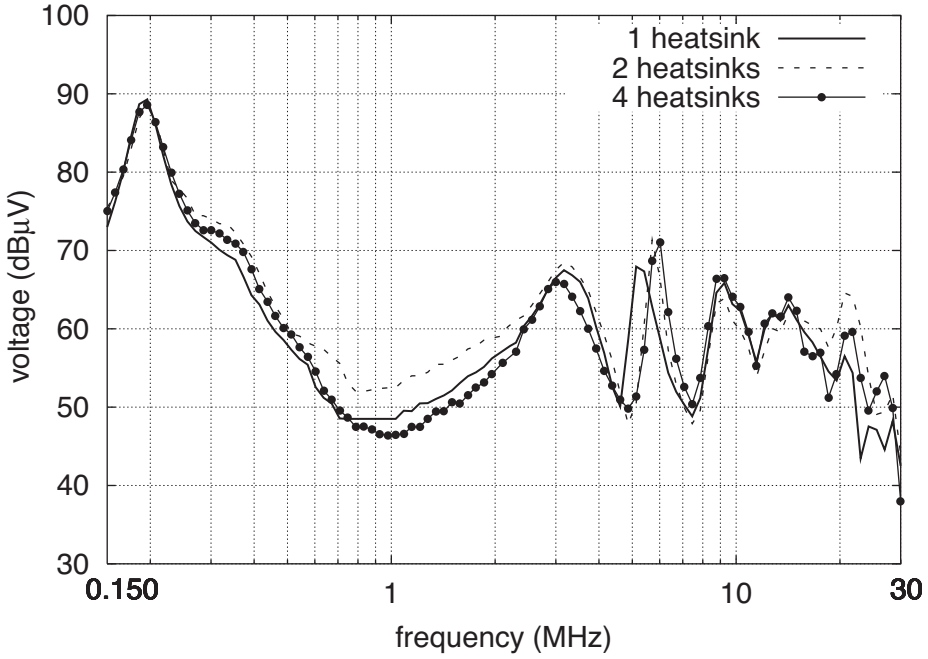

Fig. 9. DM conducted emission spectrum for ungrounded heatsinks.

At lower frequencies, the trends are consistent with the self-resonant frequencies of the DM loop formed by the input smoothing capacitor, the switches and their connecting wires, as measured with the test arrangement depicted in Figure 10.

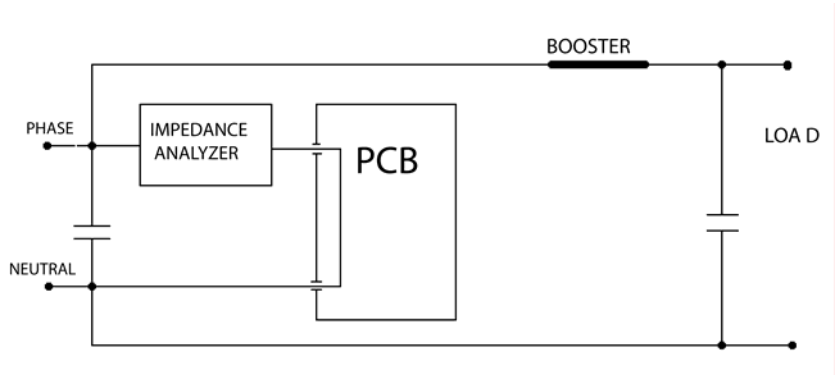

Fig. 10. Measurement setup for the self-resonant frequencies of the DM loop.

The first peak at 193 kHz, present in both grounded and ungrounded configurations, can be reconducted to DM emissions. In fact, it is still evident in Figure 8 and 9, but not in Figure 6 and 7. At higher frequencies, the trends agree with the self-resonant frequencies of the CM loop formed by the series connection of the ground wire with the parallel of the two line wires each in series with the internal stray capacitances of the SMPS. A schematic of the test arrangement for the resonant frequencies of the CM loop is shown in Figure 11.

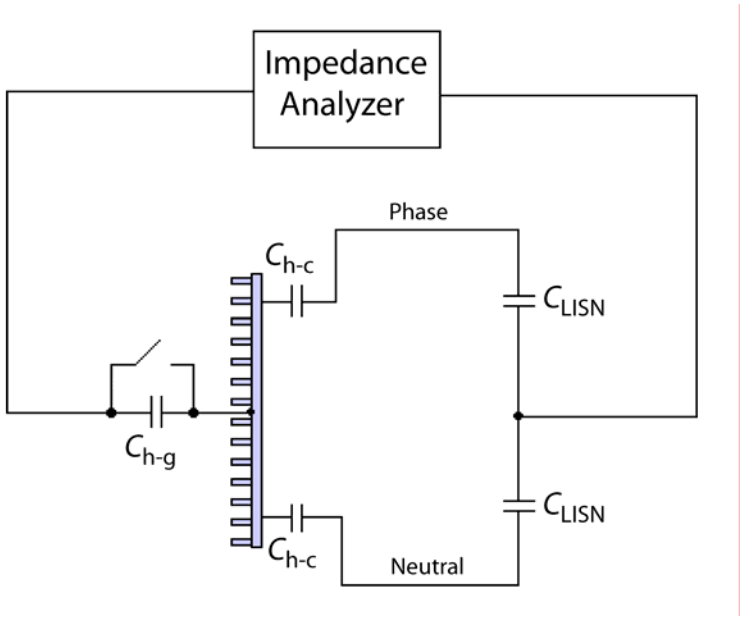

Fig. 11. Measurement setup for the self-resonant frequencies of the CM loop.

The stray capacitances between the heatsink and the collector of each IGBT are indicated with $C_{h\text{-}c}$, whereas $C_{h\text{-}g}$ is the capacitance between the heatsink and the ground. All the self-resonant frequencies of the DM and CM loops were verified with a HP4192 Impedance Analyzer. For example, three resonant frequencies (2.75, 5.6 and 8 MHz) were found in the frequency range of the analyzer (5 Hz to 13 MHz) for the grounded four-heatsink

configuration (see Figure 4). In this case, the resonant frequencies are in good agreement with the peaks of the conducted emission spectrum. Comparing Figures 6 and 7 one can notice the well known general effect of reduction of the CM component and, in turn, of the conducted emission (see Figures. 4 and 5) achieved by not connecting the heatsink to ground [3]. This is due to the reduction of the stray capacitance to ground that yields also an increase of the frequencies of the peaks.

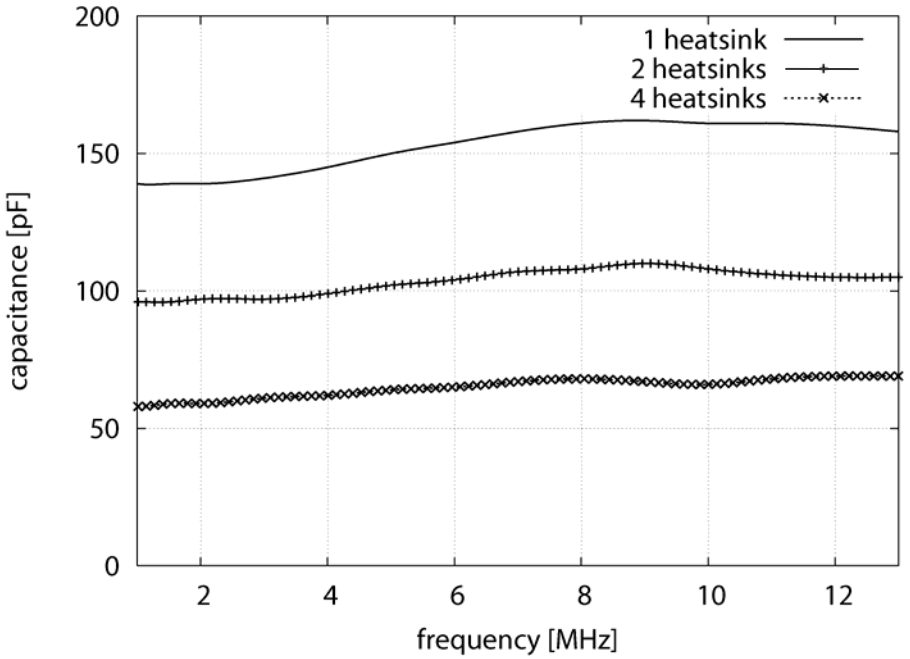

Fig. 12. Heatsink to ground stray capacitance versus frequency for the considered configurations.

Comparing the grounded configurations with the ungrounded ones, the unavoidable measurement uncertainties make hard to define which are the best configurations, except for a particular range of frequency around 5 MHz where a difference up to 10 dB can be noticed. In this frequency range there is the peak most affected by the heatsink configuration. In the ungrounded case (Figures 5 and 7) the decreased heatsink to ground capacitance due to the subdivision of the heatsink (see Figure 12) gives the best result for the four-heatsink configuration. However, this behaviour is upset in the grounded configuration because the inductance of the connection to ground plays the major role. In fact, the four wires in parallel that connect the single heatsink to the ground are reduced to two in parallel for each heatsink in the two-heatsink configuration and to one only for each heatsink in the four-heatsink configuration. In Figure 13 are shown the schematics of the ground connections and the

switching devices location on the heatsinks. The currents flowing in these ground connections generate CM voltages proportional to the relevant equivalent inductances.

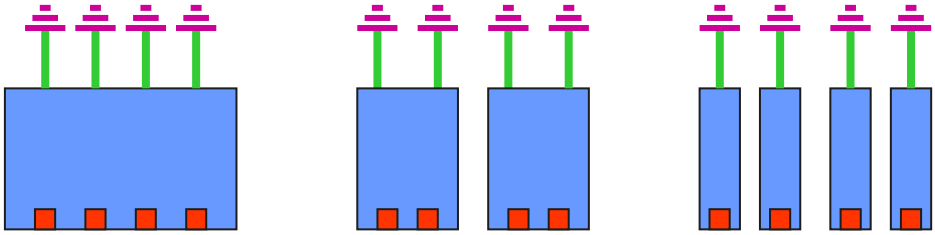

Fig. 13. Schematics of the ground connections and the switching devices location.

In Figure 14, the CM conducted emissions for the one-heatsink configuration with two and four connections to ground, respectively, are shown.

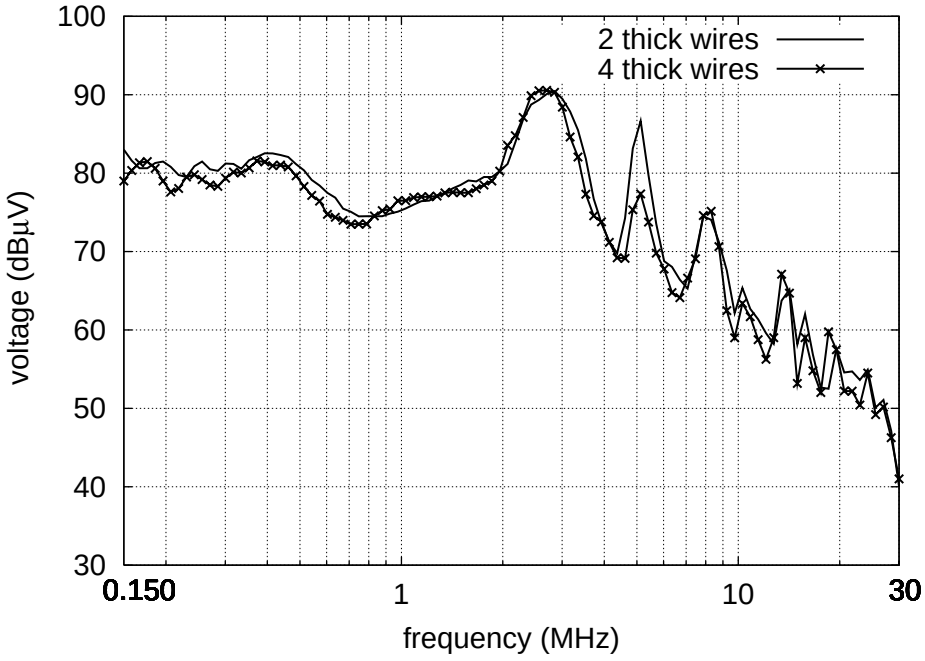

Fig. 14. CM conducted emission spectrum for one-heatsink configuration with two and four connections to ground.

The increase of the CM conducted emission for a higher inductance of the heatsink to ground connection is clearly visible around 5 MHz. From Figures 8 and 9, it can be noticed that the subdivision of the heatsink influences also the DM component of the conducted emission for frequencies higher than 500 kHz. The influence on DM conducted emission seems to be greater for the grounded configurations with two and four heatsinks for the not negligible inductance of the connection to ground, Figure 8. In fact, from the point of view of the DM

signal, the partial inductances of the ground connections in the configurations with two and four heatsinks are in series and the currents flowing in these ground connections generate DM voltages proportional to the relevant equivalent inductances. With the ungrounded heatsinks the series of the stray capacitances between a heatsink and the adjacent one leads to an equivalent impedance much higher for the DM signals (in the order of kΩ), blocking any DM currents to flow between a heatsink and the adjacent one, Figure 9.

3.2.2 Common-Mode Current Measurements

The commutation loop of the IGBTs of the voltage regulator used in the tests, includes the equivalent stray inductances of the interconnections between the snubber capacitor and the IGBTs, Figure 1. These inductances are not negligible and contribute significantly to the generation of interferences during the switching operations of the power electronic devices.
To study the CM currents from a single IGBT, the configuration with four heatsinks is adopted and a current probe is used to measure the currents flowing through the connection to ground of a single heatsink. From Figure 15, it can be noticed how the CM currents are produced and conducted to ground through the heatsink at every turn-on and turn-off of an IGBT (for instance, IGBT T1).

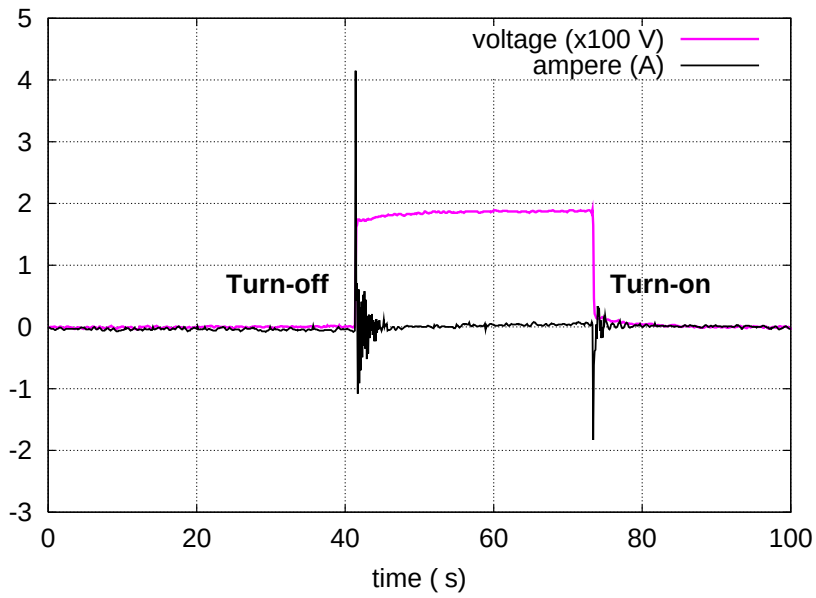

Fig. 15. Collector to emitter voltage of the IGBT T1 and relative CM currents along the connection to ground of the heatsink.

In Figure 16, the measured current waveform at the turn-off of the IGBT T1 is shown. It consists of an initial peak followed by an oscillating waveform with frequency around 5 MHz.

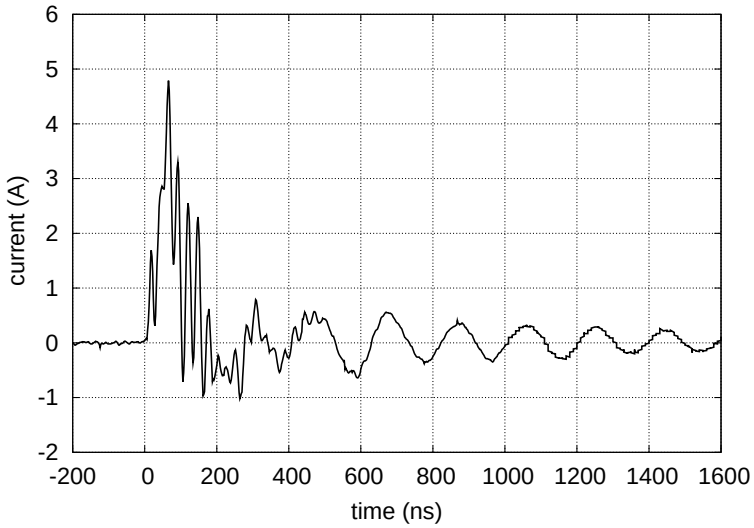

Fig. 16. Measured CM current waveform through the connection to ground of the heatsink during the turn-off of the IGBT T1.

Most of the high frequency components of these currents can be blocked placing an inductor in the connection to ground of the heatsink, Figure 17.

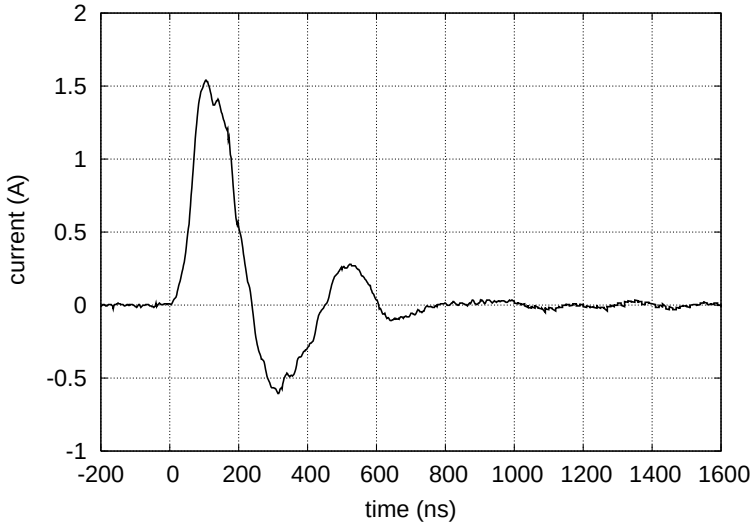

Fig. 17. Measured CM current waveform through the connection to ground of the heatsink during the turn-off of the IGBT T1, after the application of a CM inductor in the ground connection.

The inductor is constructed by winding several turns of the ground connection around a ferrite toroid with suitable characteristics over the conducted emission limit frequency range, [4]. This type of inductor is also called common-mode choke. Using a lumped inductor in the

ground connection, instead of a common-mode choke, is undesiderable because the solder joint may become defective, opening the safety wire path and leaving a potential shock hazard in case of fault. The inductance value of the common-mode choke is around 30 μH at 5 MHz. In Figure 18, the measured current waveform at the turn-on of the IGBT T1 is depicted, while Figure 19 shows the current through the same connection after placing the CM inductor in the ground connection of the heatsink**.**

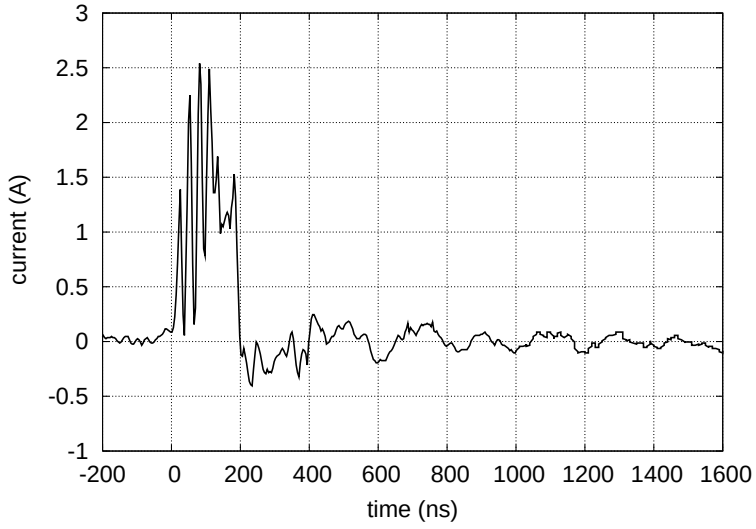

Fig. 18. Measured CM current waveform through the connection to ground of the heatsink during the turn-on of the IGBT T1.

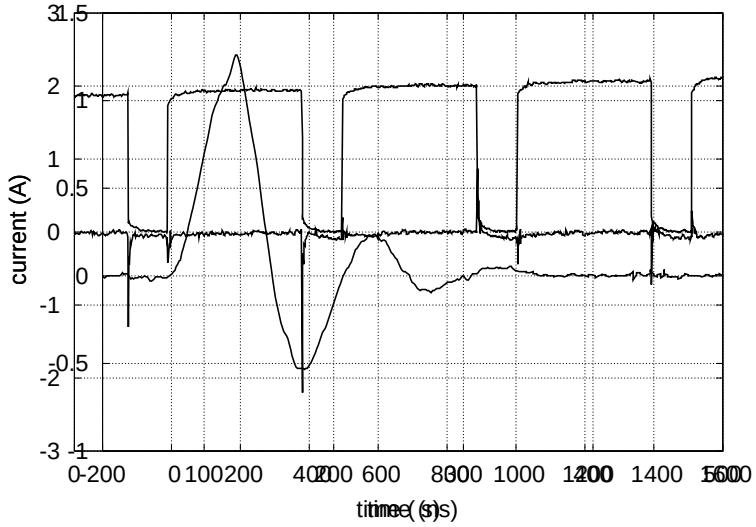

Fig. 19. Measured CM current waveform through the connection to ground of the heatsink during the turn-on of the IGBT T1 after placing an inductor in the ground connection.

Figures 20 e 21 show the measured spectra of the CM current through the connection to ground of the heatsink during the switching operations of the IGBT T1 in the frequency range 0-60 MHz and in the range 0-10 MHz, respectively. How it can be noticed, the harmonic

content of the CM current is particularly high in the range from 20 to 40 MHz. The inductor eliminates the higher harmonics of the CM current flowing through the ground connection of the heatsink.

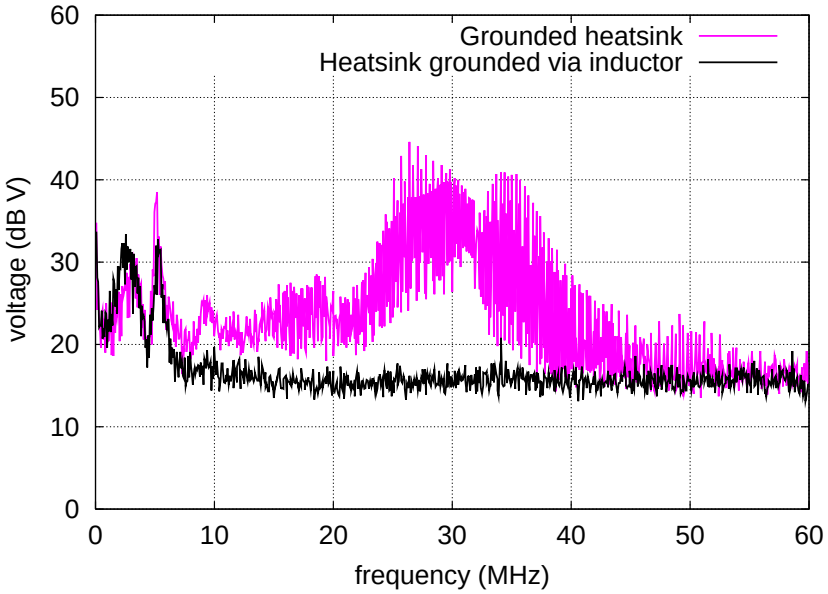

Fig. 20. Measured CM current spectrum.

At lower frequencies, the peak around 5 MHz is decreased of 10 dB with the introduction of the common-mode choke.

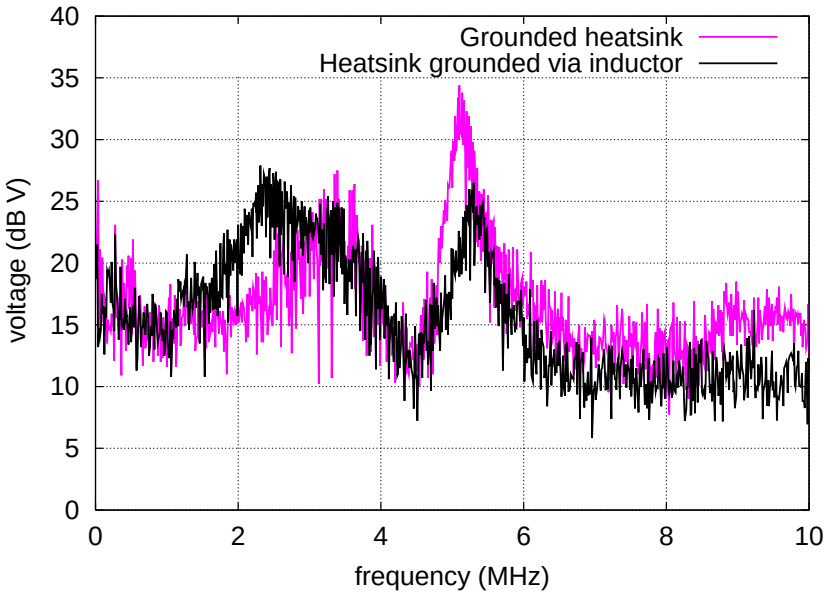

Fig. 21. Measured CM current spectrum.

In the CM conducted emission spectrum below, the peak at 5 MHz can be easily identified. However, the main frequency of disturb in the CM conducted emission spectrum is the peak between 3 and 4 MHz. This peak can be related with the initial peak of the CM current time waveform of Figure 16. In terms of conducted emission, the use of a single inductor in the ground connection of the heatsink of a single switching device (one of the four heatsinks of the configuration with four heatinks), is a convenient way to reduce EMI, Figure 22. Using a common-mode choke for each switching device of the SMPS leads to a reduction of the peak around 5 MHz, but at the same time, for the increased equivalent inductance of the ground connections, shifts the main peak of disturb towards lower frequencies. The currents flowing in these ground connections generate CM voltages proportional to the relevant equivalent inductances.

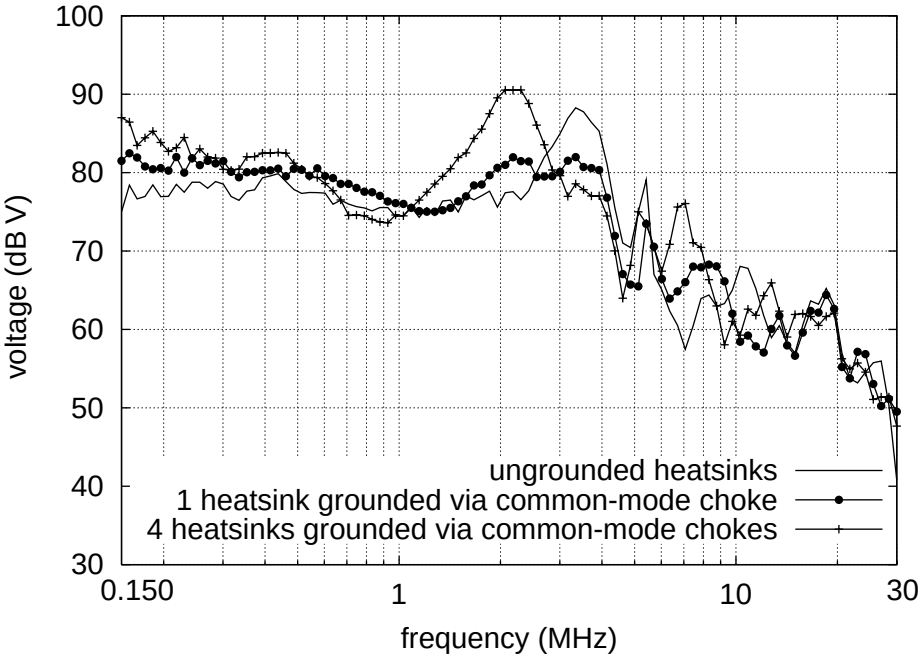

Fig. 22. CM conducted emission spectrum.

3.3 Switching Waveform of Power Electronic Devices

In power electronics, EMI sources are typically related to the switching waveform of power devices. In order to limit the CM currents at the design level of the SMPS, it's necessary to limit the overvoltages at the transistor terminals caused by the switching operations.

In this section, the model of power device switching waveform in relation to interconnection inductances is introduced. Switching waveforms are often analysed in four operating phases; turn-on transition, oscillating (ringing) phase, turn-off transition and post oscillating (ringing) phase [5], [6]. The frequency content and the amplitude of the switching waveform during the oscillating phases depend on the inductance of the interconnections and internal capacitances and resistances of the power devices in the commutation loop.

Figure 23 shows a SMPS circuit consisting of the diode-transistor commutation loop, the low-pass filter and the load. The interconnection inductance of the loop is divided into three fundamental parts: inductance between the positive pole of the battery (V_{DC}) and the MOSFET switch, L_1, inductance between the positive pole of the battery and the snubber capacitor C_s, L_2, and inductance of the common-mode return path between the drain and the negative pole of the battery, L_3.

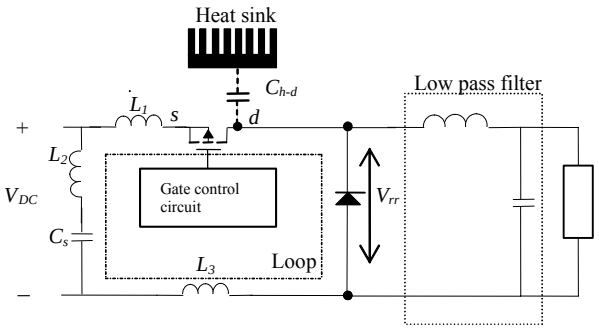

Fig. 23. Switched Mode Power Supply circuit

These parasitic inductances induce overvoltages so that the drain voltage waveform consists of transient and oscillating parts (Figure 24).

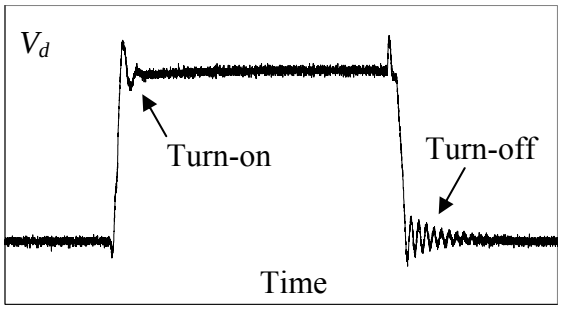

Fig. 24. Measured switching waveform (drain voltage).

During turn-on, the load current commutates from the freewheeling diode to the MOSFET. When the drain voltage reaches the supply voltage and the diode starts to recover, the MOSFET conducts and common-mode noise is produced. At this phase of the turn-on, the non linear output capacitance of the MOSFET, C_{oss}, is no longer present in the simplified circuit of Figure 25, while the diode can be replaced by its internal junction capacitor C_j.

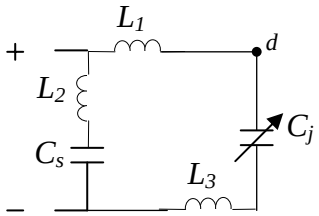

Fig. 25. HF equivalent circuit during the oscillating phase of the turn-on.

The voltage oscillations are mainly dependent on the value of L_1+L_2. The expression of the drain voltage in the frequency domain is the following:

$$V_d = j\omega \cdot \left(L_1 + L_2 - \frac{1}{\omega^2 \cdot C_s} \right) \cdot I_{loop} \qquad (1)$$

Stray inductance combined with the diode recovery *di/dt* leads to high voltage transients across the diode. For bridge configurations, such as a voltage-source inverter, this overvoltage also appears across the anti parallel transistor and can lead to junction breakdown in the power devices.

The turn-off process of the MOSFET is accompanied by a transfer of load current to the freewheeling diode. The presence of the stray inductances causes overvoltage across the transistor terminal with high frequency oscillations which increase the EMI generated by the system, Figure 24. After the drain current reaches zero a voltage ringing is observed on the

drain. The diode is now conducting and in the equivalent circuit of Figure 26, C_j is no longer present.

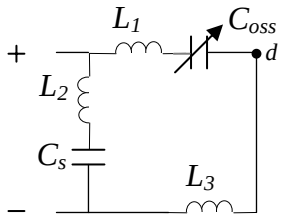

Fig. 26. High frequency equivalent circuit during the oscillating phase of the turn-off.

The ringing is strongly dependent on the value of L_3.

$$V_d = j\omega \cdot L_3 \cdot I_{loop} \tag{2}$$

If the heatsink is grounded, an insulating layer is present between the drain of the transistor and the heat sink forming a coupling path for the high frequency oscillation current generated by the drain voltage. The contribution of this capacitance to the common mode current is not negligible because its value is in the order of hundreds of pF, and the *dV/dt* produced at the semiconductor terminals is maximal.

3.3.1 Inductance Models

The significance of parasitic impedances of connecting structures in power electronics (PCB interconnects, component leads and wires) increases with frequency and influences switching transient behaviour and conducted and radiated EMI noise. Design aspects such as physical layout and interconnect routing require accurate switching waveform models and extraction of parasitic parameters. Modelling and simulation of power semiconductor device (MOSFET and diode) switching waveforms in power converter circuits are presented and discussed in [7] and [8]. The switching waveform modelling [7] is based on an expression for overvoltage during MOSFET turn-off which incorporates stray inductance as a parameter in the circuit design. The stray inductance is computed by the Partial Element Equivalent Circuit (PEEC) method which attributes a certain amount of inductance and resistance to each part of a conductive structure. This results in a lumped parameter circuit model which describes the

circuit behaviour due to parasitics and can be easily implemented in SPICE simulations. The other approach is to model typical power electronic interconnections as RLC ladder networks (T or Π-networks) [8]. Interconnection parameters are calculated by inductance, capacitance and resistance analytical formulae of planar and round conductors over ground planes. The advantage of using analytical formulae for the design is in their direct relation to the physical dimensions of the connecting structures.

Power PCB connecting structures are less complex than Very Large Scale Integrated (VLSI) interconnections but with increasing frequency the size of power converter circuits and metallic structures becomes comparable with signal wavelengths thus numerical approaches become essential as is the case with VLSI circuits. Currently, electromagnetic field simulators based on numerical methods are used to analyse EM behaviour and to extract parasitic inductance of power PCBs. However, EM simulations may require long computing time due to large topologies of printed conductors with multiple access points. Therefore analytical and numerical EM methods are combined to adopt the most suitable method for each specific PCB topology [9] in order to conciliate the reduction of computing time with reasonably accurate EM analysis.

In the following two subsections the analytical and numerical inductance models for two circuit topologies (PCB traces) are described.

A. Lumped Models: Transmission Line Method

The transmission line models used are based on a PCB layout with large copper lands and a layout with ordinary traces. The layout with the large copper lands corresponds to a coplanar waveguide and the layout with the ordinary traces corresponds to a coplanar strip (Figure 27).

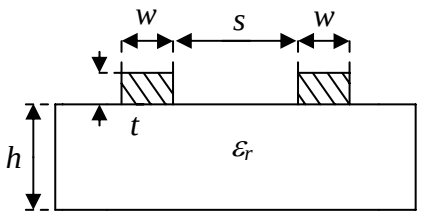

(a)

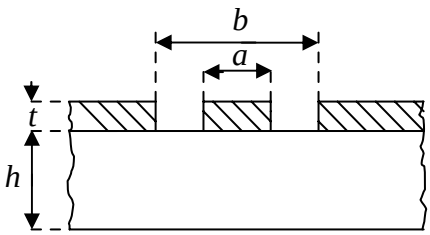

(b)

Fig. 27. PCB layouts: (a) coplanar strips, (b) coplanar waveguide.

A coplanar strip structure typically represents power converter PCB lands (Figure 27a). Partial inductance formulae [10], [11]:

$$L_p \cong 2\times10^{-7} l\left[\ln\left(\frac{2l}{w}\right)+\frac{1}{2}\right] \tag{3}$$

$$M_p \cong 2\times10^{-7} l\left\{\ln\left[\frac{l}{s}+\sqrt{\left(\frac{l}{s}\right)^2+1}\right]+\frac{s}{l}-\sqrt{\left(\frac{s}{l}\right)^2+1}\right\} \tag{4}$$

are used to estimate the trace inductances, taking into account the width w, length l and distances s of the traces where L_p and M_p represent the self and mutual partial inductance between PCB lands for $l/w >> 1$. Thus, the inductance per unit length can be simply multiplied by the length of the three fundamental interconnections.

The characteristic impedance and inductance per unit length of a coplanar waveguide layout (Figure 27b) can be calculated by the formulae [12] given in the Appendix. Table 1 shows the calculated inductances.

Table 1. Calculated Interconnection Inductances

Interconnections inductance	Coplanar strip-line	Coplanar waveguide
L_1 [nH]	58	29
L_2 [nH]	50	13
L_3 [nH]	158	61

B. Distributed Models: the FE and FDTD Methods

This section presents the distributed models of stray inductance in the switching circuit. The model is based on the loop inductance concept [13] that is adopted and analysed in [14]. Unlike partial inductance approach [15], this approach focuses on the high frequency equivalent circuit formed of the diode-transistor commutation loop as it is explained in Section 3.2. The diode-transistor commutation loop is modelled using the FDTD [16], and FE (High Frequency Simulation, HFSS), [17] methods.

The FDTD technique divides the computational space up into cubic cells with the electric and magnetic fields discretised in the manner of these cells. The fundamental constraint on the cell size is that it must be much less than the smallest wavelength for which accurate results are desired. Moreover, in our geometries, the cell size cannot be bigger than 2 mm to properly design the tracks width and the cell size width. Liao absorbing boundary condition [16] are used to the outer boundary. The selection of the waveforms depends on the required output results. Hence, in this paper we use a Gaussian pulse to provide a broadband input which is suitable for typical output results versus frequency, such as input impedance computations. The pulse width and the simulation time steps are chosen in order to get the voltage port signal attenuated to zero by the end of the simulation. To analyze the inductance of a loop, the voltage and the current time waveform are monitored at the excitation port and later processed and transformed into the frequency domain. The input impedance of the system is calculated from the voltage-to-current ratio:

$$Z(j\omega) = \frac{V(j\omega)}{I(j\omega)} \tag{5}$$

The HFSS technique is based on the Finite Element Method and scattering parameter analysis [17]. The FEM is one of the known methods for the solution of partial differential equations in applied mathematics and computational mechanics. Unlike the FDTD method, where the computational space is divided into cubic cells, the FEM permits very general geometrical elements and usually only uses one grid. The HFSS code meshes the structure automatically, and then refines the mesh until a negligible change in S-parameters is reached from one iterative pass to the next. To compute the input impedance, the scattering parameters are calculated at the excitation port and then converted in Y and Z parameters in the frequency domain.

In order to examine how the stray inductance of complex loops influences EMI we apply FDTD and HFSS modelling to a coplanar strip layout (Figure 28) and to a coplanar waveguide layout (Figure 29) of the same diode-transistor commutation loop circuit. In the FDTD model, the computational space consists of 110×80×40 cells of 2×1×1 mm size and the excitation source is a Gaussian pulse. In HFSS model the solution frequency is 100 MHz and the total size of the computational space is 200× 200×40 mm.

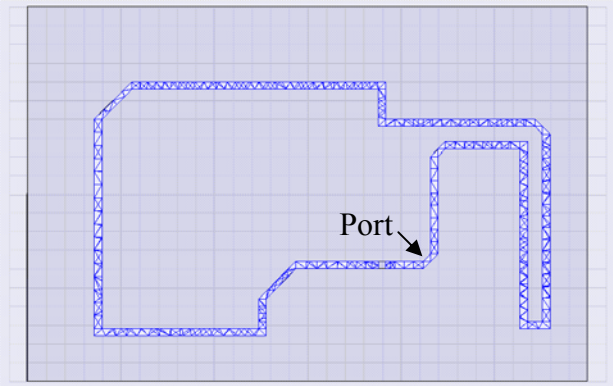

Fig. 28. Coplanar strip PCB layout (HFSS).

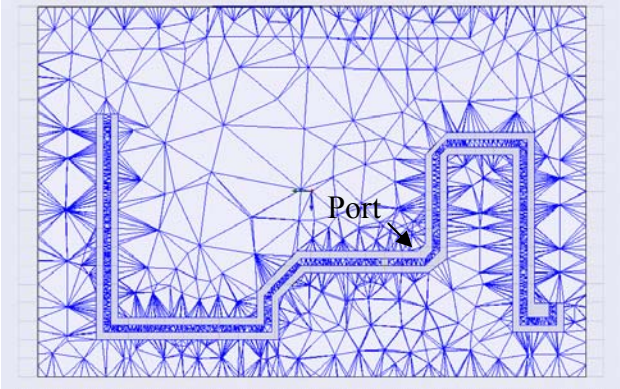

Fig. 29. Coplanar waveguide layout (HFSS model).

The imaginary part of the input impedance (5) is computed over the frequency range 150 kHz-50 MHz, which is big enough to contain the frequency content of the conducted emission from SMPS [18]. In this range the impedance trends are linear (Figure 30) therefore the overall inductance can be treated like the sum of three components as it is shown in Section II. The real part of the input impedance is negligible in the frequency range under study if compared with the internal drain to source resistance of the main switching device. The extracted coplanar strip inductance is 270 nH while the coplanar waveguide inductance is 103

nH. These values are in good agreement with those calculated by analytical formulae and shown in Table 1. This shows that the stray inductance can be reduced significantly when the coplanar waveguide traces are used in the layout.

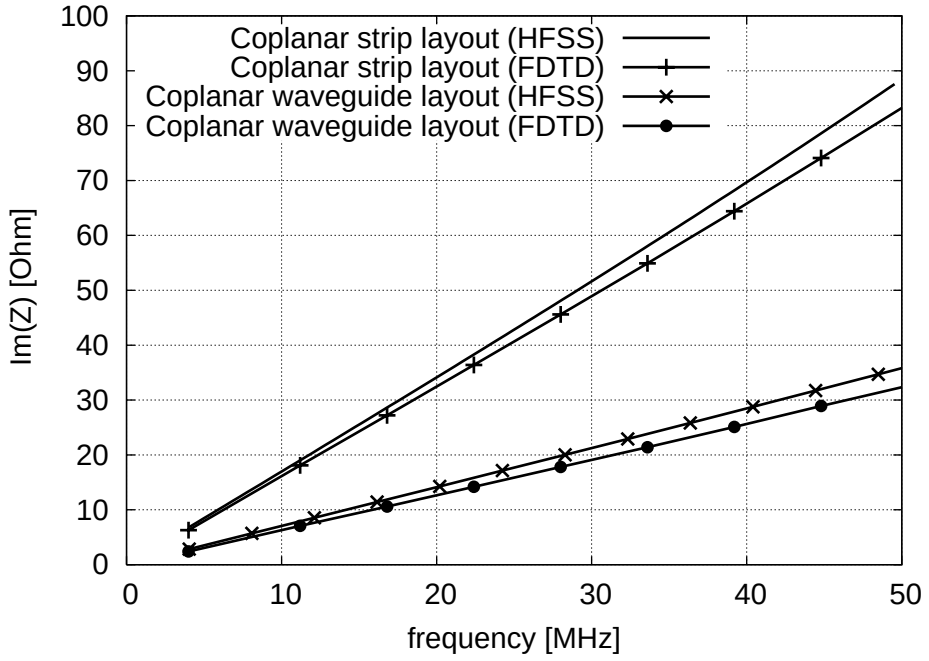

Fig. 30. Imaginary part of the input impedances for the FDTD and HFSS models.

The distributed inductance models in this section are limited to specific topologies and do not take into account the real return current path that contributes to the interconnection inductance.

3.3.2 Circuit Simulations and Measurements

In order to model switching waveforms of the SMPS circuit and relate them to the stray inductance of the commutation loop, the values of the extracted inductances are inserted together with the internal capacitances of the devices in the PSPICE circuit (Figure 31). The MOSFET and diode parameters are taken from the datasheets [19] and inserted through the model editor in the general device models [20]. The values of the MOSFET switch and drain lead inductances are also introduced in the model. The control section is simulated by an equivalent square wave pulse generator V_g supplying the gate of the switching element.

In the experimental layout the gate wires are located as far as possible from the commutation loop to avoid inductive coupling. Internal series inductance and resistance of the electrolytic capacitor has been neglected for the low value of the snubber capacitor. The adopted probe is a Tektronix P6245 voltage probe with bandwidth from dc to 1.5 GHz. Since the heat sink has no influence on the measured results, we do not include it in the PSPICE circuit.

The PSPICE simulations are compared with the measurements of the drain voltage between the node *d* and the negative pole of the battery, during the oscillating phase of the turn-on and the turn-off.

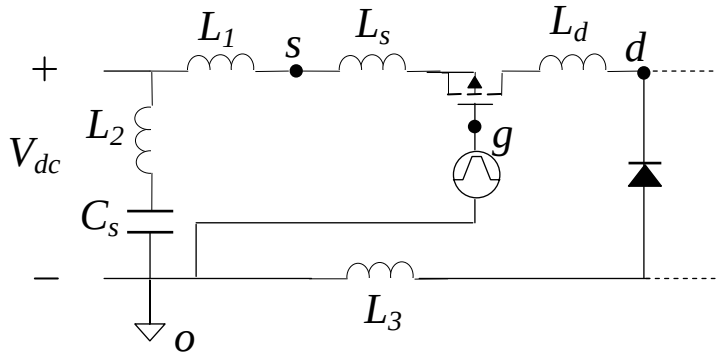

Fig. 31. PSPICE simulation circuit of a buck converter.

Simulation and measurement results for the coplanar strip layout are shown in Figure 32 and 34. The frequency of voltage oscillations during turn-off is about 17.5 MHz that corresponds to a period of the drain voltage ringing of 57 ns.

Figures 33 and 35 show the simulated and measured results for the coplanar waveguide layout. The period of the drain voltage oscillations at turn-off is about 35 ns that correspond to a maximum frequency of 28 MHz.

Simulated waveforms of Figure 32 and 33 show the additional high frequency ringing due to the oscillating current on the diode during the reverse recovery time. The junction capacitance of the diode is 15 pF. This value strongly influences the duration and the amplitude of this secondary ringing.

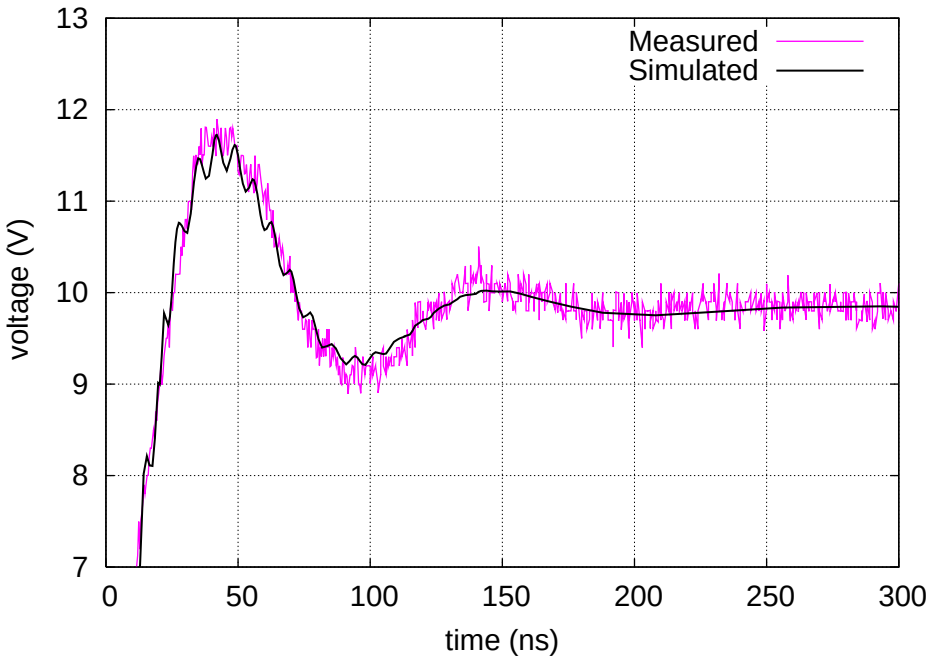

Fig. 32. Switching waveform during turn-on (coplanar strip layout).

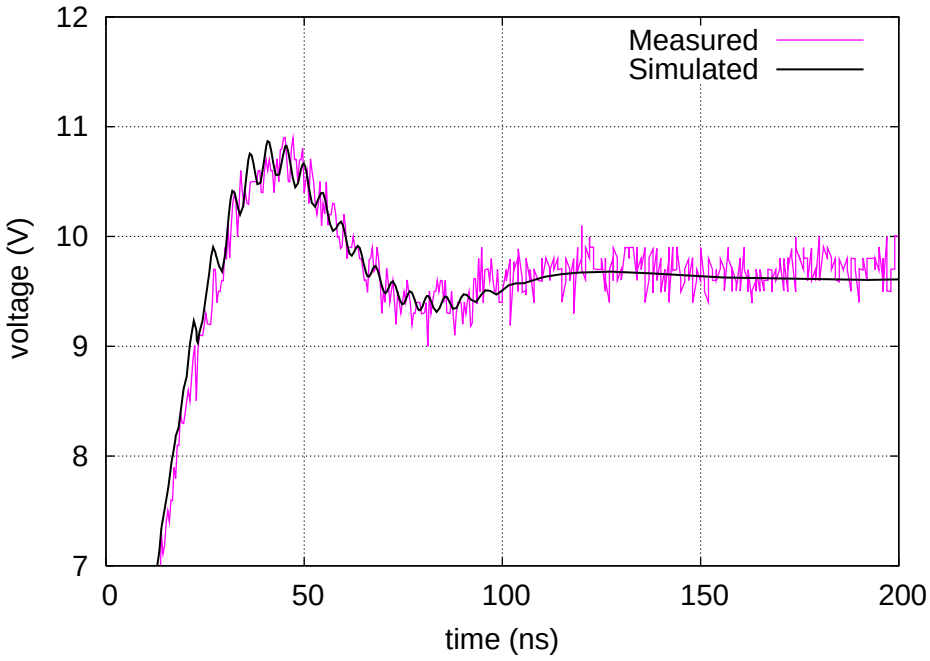

Fig. 33. Switching waveform during turn-on (coplanar waveguide layout).

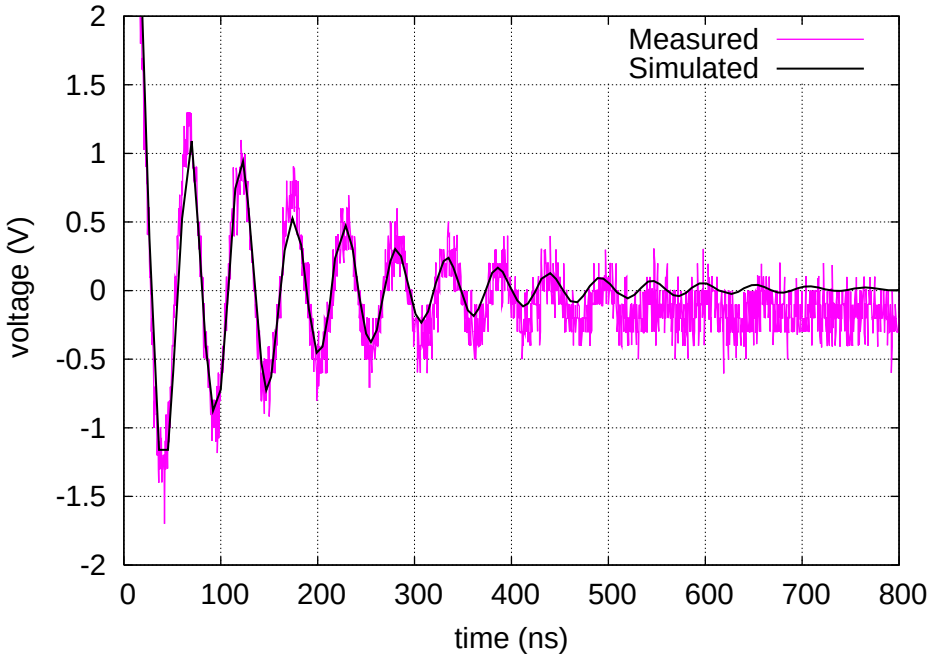

Fig. 34. Switching waveform during turn-off (coplanar strip layout).

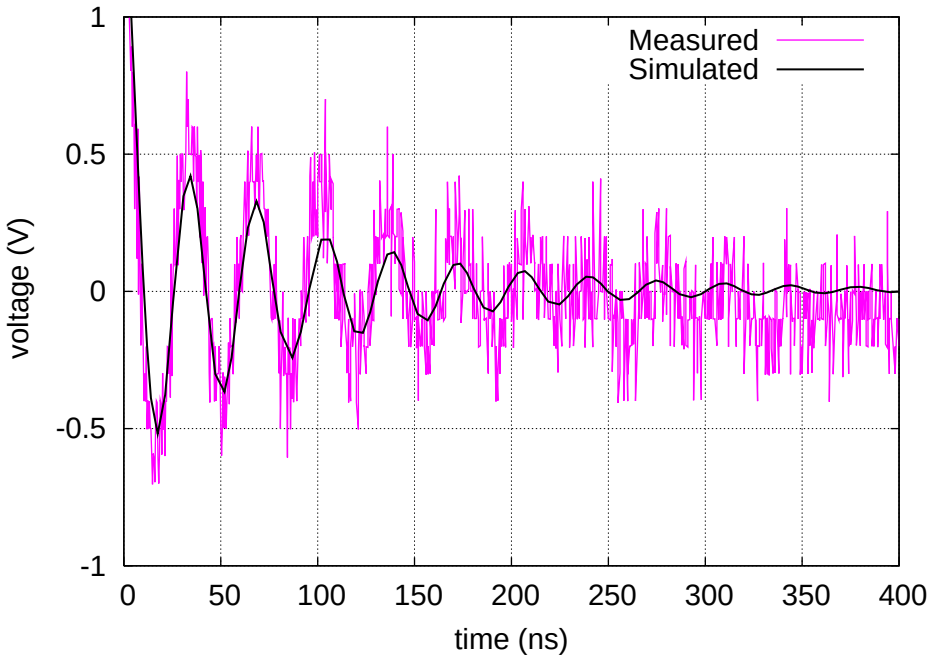

Fig. 35. Switching waveform during turn-off (coplanar waveguide layout).

The PSPICE simulations match well with the measurements of the drain voltage. The amplitude and the oscillating period of the drain voltage waveform increase proportionally with the loop inductance. In particular, it is shown that the turn-on waveform depends on the inductance between the switch and the bus DC, while the turn-off waveform is dependent on the inductance of the return path.

3.3.3 Common-Mode Current Calculation

The CM current flowing through the connection to ground of the heatsink is related with the drain voltage (Figure 31), by the following relation in the frequency domain:

$$I_{CM}(s) = \frac{V_{d-o}(s)}{Z_{d-o}(s)} = \frac{V_{d-o}(s)}{sL_{h-o} + \frac{1}{sC_{h-d}}} \tag{6}$$

where $Z_{d\text{-}o}$ is the impedance formed by the series of the stray capacitance ($C_{h\text{-}d}$), introduced by the thin insulating layer located between the heatsink and the MOSFET (Figure 23), and the self partial inductance of the grounding connection of the heatsink $L_{h\text{-}o}$ [10].
For a unit impulse voltage, expression (6) become:

$$I_{CM}(s) = \frac{1}{sL_{h-o} + \frac{1}{sC_{h-d}}} = \frac{1}{L_{h-o}} \cdot \frac{s}{s^2 + \frac{1}{L_{h-o}C_{h-d}}} \tag{7}$$

The Inverse Fourier Trasform is given by:

$$i_{CM}(t) = \frac{1}{L_{h-o}} \cdot \cos(\omega_{d-o} t) \tag{8}$$

with

$$\omega_{d-o} = \frac{1}{\sqrt{L_{h-o}C_{h-d}}}$$

During the oscillating phase of the turn-off of the MOSFET in the SMPS of Figure 23, the excitation signal waveform is a damped sinusoid (Figure 34):

$$v_{d-o}(t) = \exp^{-at} \cdot sen(\omega t) \tag{9}$$

The substitution of the FFT of (9) into equation (6) yields the following expression:

$$I_{CM}(s) = \frac{\dfrac{\omega}{(s+a)^2+\omega^2}}{sL_{h-o} + \dfrac{1}{sC_{h-d}}}$$

The theory of partial fractions allows this complicated fractional value to be decomposed into a sum of small, simple fractions.

To calculate the common-mode current due to the oscillating phase of the turn-off of the MOSFET in the SMPS with coplanar strips (Figure 34), the following parameters are introduced:

$\omega = 2\pi \cdot 17e6\, {rad}/{\sec} \approx 10^7\, {rad}/{\sec}$

$a = 7\mathrm{e}^6$

$L_{h\text{-}o} = 5$ nH (calculated)

$C_{h\text{-}d} = 150$ pF (measured)

$$I_{CM}(s) = \frac{\dfrac{\omega}{(s+a)^2+\omega^2}}{sL_{h-o} + \dfrac{1}{sC_{h-d}}} = \frac{\omega}{s^2+a^2+2sa+\omega^2} \cdot \frac{sC_{h-d}}{s^2 L_{h-o} C_{h-d} + 1} = \frac{\omega}{s^2+a^2+2sa+\omega^2} \cdot \frac{\dfrac{s}{L_{h-o}}}{(s^2+\omega^2{}_{d-o})} =$$

$$= \frac{2e^{16} \cdot s}{\left(s^2+1e^{16}+14e^6 s\right)\cdot\left(s^2+133.3e^{16}\right)} = \frac{As+B}{s^2+1e^{16}+14e^6 s} + \frac{Cs+D}{s^2+133.3e^{16}}$$

The constants *A, B, C* and *D* can be determined by using an algebric method.

$$I_{CM}(s) = \frac{0.015s - 12.29e^6}{s\ +1e^{16}+14e^6 s} - \frac{0.015s+713e^4}{s^2+133.3e^{16}}$$

The common-mode current in the frequency domain can be written in the following form:

$$I_{CM}(s) = 0.015\cdot\frac{s+7e^6}{\left(s+7e^6\right)^2+(1e^8)^2} - 0.24\cdot\frac{1e^8}{(s+7e^6)^2+(1e^8)^2} - 0.015\cdot\frac{s}{s^2+(1.15e^9)^2} - 0.0062\cdot\frac{1.15e^9}{s^2+(1.15e^9)^2}$$

Doing the inverse Fourier transform of each term, the time waveform for the calculated common-mode current become:

$$i_{CM}(t) = 0.015 \cdot \exp(-7e^6 t) \cdot \cos(1e^8 t) - 0.124 \cdot \exp(-7e^6 t) \cdot sen(1e^8 t) - 0.015 \cdot \cos(1.15e^9 t) - 0.0062 \cdot sen(1.15e^9 t) \text{ A}$$

Figures 36 and 37 show the time waveform of the common-mode voltage during the oscillating phase of the turn-off and the calculated common-mode current flowing through the grounding connection of the heatsink.

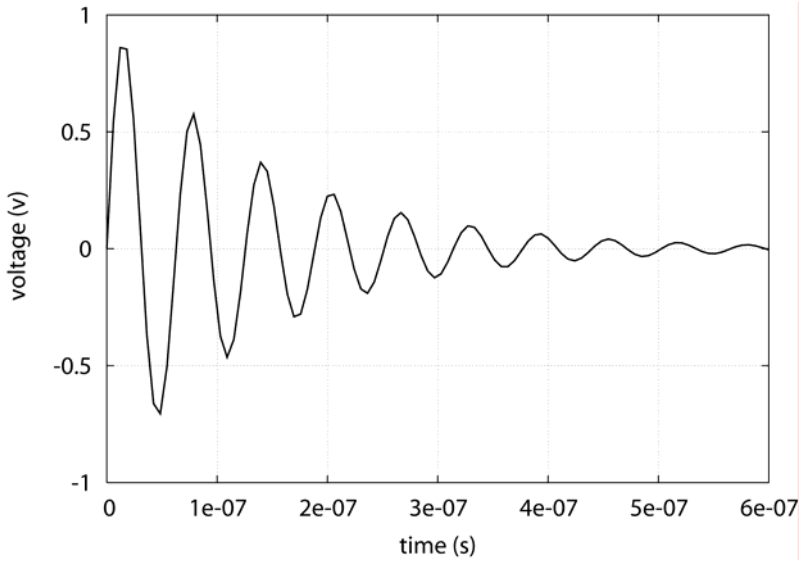

Fig. 36. Common-mode voltage during the oscillating phase of the turn off.

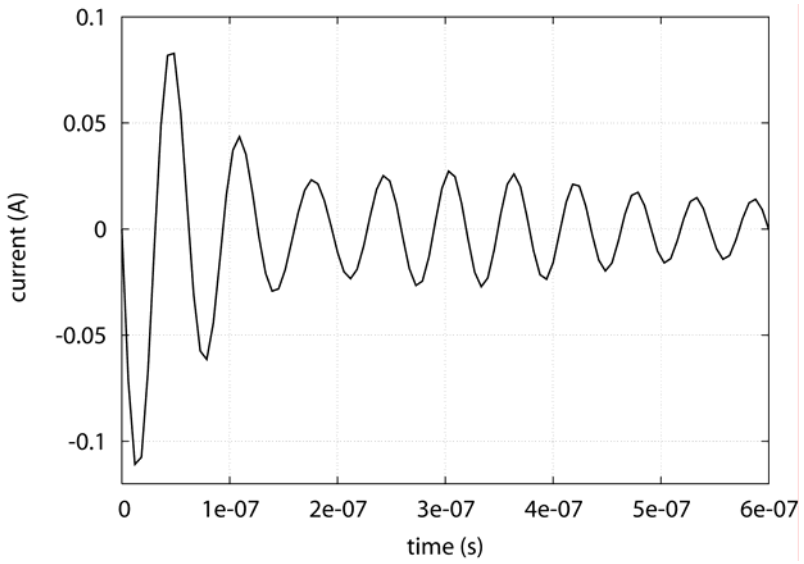

Fig. 37. Common-mode current during the oscillating phase of the turn off.

3.4 Summary

The influence of different heatsink configurations for SMPS on conducted EMI and on its CM and DM components is considered in the first part of the chapter. It is emphasized the effect of the stray capacitances introduced by three different heatsink configurations through conducted EMI measurements. The comparison shows only slight differences among conducted emission measurements for the considered heatsink configurations. The difference of few dB among the results may be confused with measurement errors. However, for a little range of frequency around 5 MHz, changes in the heatsink configuration lead to variations up to 10 dB, giving the ungrounded four-heatsink configuration the lowest emission. The advantage of reduction of the stray capacitance to ground is lost in the grounded configuration due to the not negligible inductance of the connection to ground.

The main frequencies of disturb in the CM conducted emission spectrum can be reduced by subdividing the heatsink among the switching devices of the main commutation loop, and by using a common-mode choke on the connection to ground of one heatsink. This new filtering technique is verified by experimental results. Using a common-mode choke for two or more switching device can leads to a saturation of the inductor, while using a common-mode choke for each switching device increase the overall impedance of the connections to ground.

The objective of the second part of the chapter is to study and predict the effects of power PCB interconnection inductances on the switching waveform of the power device. In order to limit the CM currents at the design level of the SMPS, it's necessary to limit the overvoltages at the transistor terminals caused by the switching operations. A modelling solution that focuses on the high-frequency equivalent circuit of the power supply is proposed. Since in the frequency range of 150 kHz-50 MHz the interconnection impedance trends are linear, lumped inductance models are used in the equivalent circuit.

The simulation of complex topologies in power electronics requires the prediction of EM coupling effects. Therefore, distributed models of stray inductance for coplanar strip and coplanar waveguide topology of the switching circuit are also investigated using the FDTD and HFSS based simulations.

The described and proposed modeling technique is verified by measurements and PSPICE simulations. Overall, the results validate the use of HF equivalent circuit and lumped inductance models for the design of power electronic circuits.

The results in this chapter were published by the author in [18] and [21].

Appendix

Calculation of the coplanar waveguide transmission line parameters [12]

1) Calculation of geometrical parameters of coplanar waveguide see Fig. 5b.

$$k = \frac{a}{b}$$

$$k' = \sqrt{1.0 - k_t^{\,2}}$$

$$k_t = \frac{a_t}{b_t}, k_t^{'} = \sqrt{1.0 - k_t^{\,2}}$$

$$k_1 = \frac{\sinh\left(\frac{\pi a_t}{4.0h}\right)}{\sinh\left(\frac{\pi b_t}{4.0h}\right)}, k_1' = \sqrt{1.0 - k_1^{\,2}}$$

$$a_t = a + \frac{1.25t}{\pi}\left[1.0 + \ln\left(\frac{4.0\pi a}{t}\right)\right]$$

$$b_t = b - \frac{1.25t}{\pi}\left[1.0 + \ln\left(\frac{4.0\pi b}{t}\right)\right]$$

2) Calculation of characteristic impedance and effective permittivity

$$Z_0 = \frac{30.3\pi}{\sqrt{\varepsilon_{eff,t}}}\frac{K(k_t^{'})}{K(k_t)}$$

$$\varepsilon_{eff,t} = \varepsilon_{eff} - \frac{\varepsilon_{eff} - 1.0}{\frac{(b-a)/2.0}{0.7t}\frac{K(k)}{K(k')} + 1}$$

$$\varepsilon_{eff} = 1.0 + \frac{\varepsilon_r - 1.0}{2.0}\frac{K(k')K(k_1)}{K(k)K(k_1^{'})}$$

$$K(k) = \sqrt{1.0 - k^2}$$

$$\frac{K(k)}{K(k')} \cong \frac{2.0\pi}{\ln\left(2.0\frac{\sqrt{1.0+k'} + \sqrt[4]{4.0k'}}{\sqrt{1.0+k'} - \sqrt[4]{4.0k'}}\right)}$$

References

[1] G. Grandi, I. Montanari and U. Reggiani, "Effects of power converter parasitic components on conducted EMI," in *Proc. Int. Zurich Symp. EMC*, Zurich, Switzerland, February 1996, pp. 499–504.

[2] T. Guo, D. Y. Chenand F. C. Lee, "Separation of the common-mode and differential-mode conducted EMI noise," *IEEE Transactions on Power Electronics*, vol. 11, no. .3, May 1996, pp. 480–487.

[3] L. Tihanyi, *Electromagnetic compatibility in power electronics*, J. K. Eckert & Company, Inc., Sarasota, Florida, USA, 1995.

[4] R. Lee Ozenbaugh, *EMI Filter Design*, 2nd Edition, Marcel Dekker, Inc., New York, USA, 2001.

[5] N. Mohan, T. M. Undeland, W. P. Robbins, *Power electronic: converters applications and design*, John Wiley and Sons, New York, 1989.

[6] Y. Ren, M. Xu, J. Zhou, F.C. Lee, "Analytical loss model of power MOSFET" , *IEEE Transactions on Power Electronics*, Vol. 2, March 2006, pp. 310-319.

[7] Teulings W., J.L. Schanen, J. Roudet, "Mosfet switching behavior under influence of PCB stray inductance", in *Proc. thirty-first IAS annual meeting*, vol. 3, October 1996, pp. 1149-1153.

[8] Van Wyk jr J.D. et al., "Converter Parasitics-extraction, modeling and utilization: an overview", *AFRICON*, *1999 IEEE*, vol. 2, September - October 1999, pp. 599-604.

[9] Guen A. G., Costa F., Labarre C., 'Hybrid Modelling Techniques for Multilayered Printed Circuit Board in Power Electronics: Association of Electromagnetic Methods, *IEEE Transactions on Electromagnetic Compatibility*, Vol. 46., No. 4, November 2004.

[10] C. R. Paul, *Introduction to Electromagnetic Compatibility*, Wiley, New York, 1992.

[11] F.B.J. Leferink, "Inductance calculations; methods and equations", *IEEE International Symposium on Electromagnetic Compatibility*, August 1995, pp. 16-22

[12] B.C. Wadell, *Transmission line design handbook*, Artech House, Boston, 1991.

[13] M. Bueno and A. K. T. Assis, 'Equivalence between the formulae for inductance calculation', *Canadian Journal of Physics*, Vol. 75, 1997, pp. 357-362.

[14] G. Felic, R. Evans, "An approach to inductance modelling for power PCB interconnections", *VI International Symposium on Electromagnetic Compatibility and Electromagnetic Ecology*, St. Petersburg, Russia, June 2005.

[15] A.E. Ruehli, C. Paul, J. Garrett, “Inductance calculations using partial inductances and macromodels”, *IEEE International Symposium on Electromagnetic Compatibility*, August 1995, pp. 23-28.

[16] K. S. Kunz and R. J. Luebbers, *The finite difference time domain method for electromagnetics*, CRC, Boca Raton, 1993.

[17] Ansoft Corporation (HFSS), www.ansoft.com.

[18] A. Dolente, U. Reggiani and L. Sandrolini, “Analysis of the heatsink influence on conducted EMI generation in SMPS”, *XVI International Symposium on Electromagnetic Compatibility*, Zurich, Switzerland, February 2005.

[19] *International Rectifier Databook, 1985.*

[20] Circuit analysis reference manual, circuit analysis users’ guide with schematics, April 1995. MicroSim PSpice.

[21] A. Dolente, G. Felic, “A Modelling Technique for Power Printed Circuit Board in Power Electronics”, *EMC society Australia*, 2006.

CHAPTER 4

“Radiated Emissions from Heatsink”

4.1 Introduction

In switched-mode power supplies (SMPS), many switching devices (IGBTs and MOSFETs) are usually mounted on a single heatsink. This kind of supply may be the source for common-mode currents that can find in the heatsink a path to the ground. The surface current density distribution on the heatsink radiates also fields in the near- and far-field regions. Although to a lesser extent, SMPS are in fact a reason for concern also for radiated emissions [1]. Even though the switching frequency of the devices is in the order of tens of kilohertz, unwanted radiated emissions can be expected in a broad frequency range [2]. This chapter investigates by means of numerical simulations the influence that different heatsink configurations have on the generation of radiated emission. The effects of a subdivision of the heatsink among the different switching devices of a SMPS are examined. The plots of the electric near and far field for different excitation conditions are analyzed.

4.2 Application of Numerical Methods

Electronic systems are moving toward higher circuit complexity with faster operating frequencies and consequent rapidly increasing generation of electromagnetic compatibility issues. The increased switching frequency greatly increases the significance of the inevitable structural inductances and capacitances. Parasitic effects in power electronic converters are associated with structures such as Power Circuit Board (PCB) interconnects, heatsinks and semiconductor packages. Hence the 3D Maxwell equation based computational tools that extract electromagnetic parasitic parameters become an integral part of the design methodology.

Electromagnetic parameters can be estimated using different computational tools and methods. The common tools for electromagnetic analysis used in power electronics are based on the Partial Element Equivalent Circuit (PEEC) and Finite Element (FE) methods. The PEEC method models interconnections (conductors) as partial inductors and resistors which become directly available for automatic insertion into a netlist readable by SPICE programs enabling simulations of power converters that include the influence of interconnects [3]. The use of this method provides a solution in the form of an equivalent circuit.

The 3D FE method used to solve the Maxwell equations in the harmonic time behaviour is not suitable when parameter estimates over a wide frequency range are needed. Time-domain computations suit the transient nature of power electronic systems and time-domain data can be easily converted into the frequency domain.

The Finite Integral Technique (FIT) is the method of choice in this thesis to investigate the radiated emissions from heatsink. First proposed by Weiland in 1976/1977 [4], FIT provides a universal spatial discretization scheme, applicable to various electromagnetic problems, ranging from static field calculations to high frequency applications. The spatial discretization of the integral form of the Maxwell's equations is performed on two orthogonal grid systems, created by splitting up the calculation domain into several small cuboids. It can work with a wide range of stimuli (disturbance sources), objects, environments and response locations and provides transient electromagnetic solutions for complex systems with a wide range of objects (conductors, dielectrics and metallic bodies). These capabilities make FIT applicable to electromagnetic modelling of power electronic systems that operate with naturally generated transient effects.

4.3 Modelling of Heatsink Electromagnetic Characteristics

Three heatsink structures are examined: a single heatsink with four sources, two heatsinks with two sources each, and four heatsinks with one source each. The heatsink structures considered in the simulations are shown in Figure 1. The two- and four-heatsink configurations are obtained subdividing the width of the single heatsink in two and four equal parts, respectively. In order to simulate the ground reference plane, the base of the mesh region is modelled as a perfect conductor, whereas open space conditions are satisfied on the other mesh region boundaries. The distance between the ground plane and the heatsinks is

fixed to 3 cm, according to the separation distance between the PCB and the heatsinks in the voltage regulator used in the tests. To represent the collector to emitter voltage of each transistor a discrete source (port) is added between the heatsink and the ground plane.

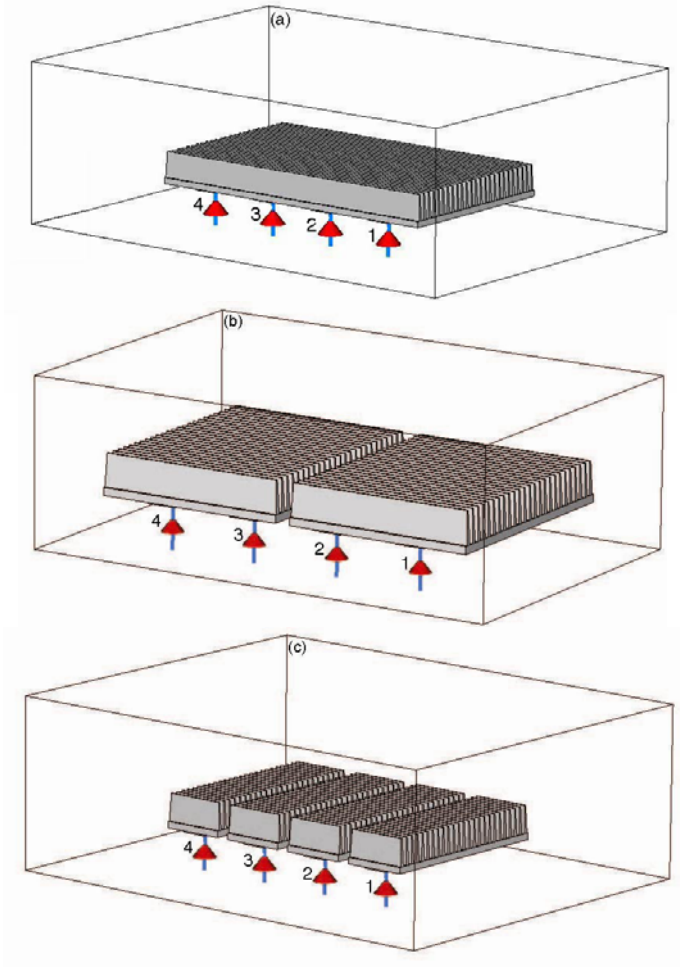

Fig. 1. Heatsink configurations examined. (a) One-heatsink structure (255x150x25 mm), (b) two-heatsink structure (2x120x150x25 mm), (c) four-heatsink structure (4x55x150x25 mm).

This port type is modelled by a lumped element, consisting of a current source with an inner impedance, which excites and absorbs power, Figure 2. The current source will only be active, when the discrete element is the stimulation port in the transient analysis. This port realizes an input power of 1W.

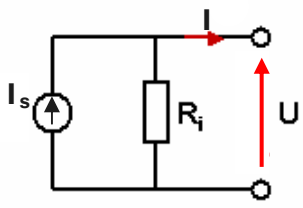

Fig. 2. Stimulation port

Each structure is excited by a sequence of four pulses simulating the generation of high-frequency harmonics of switching currents in the IGBTs of the SMPS considered. The behaviour of the heatsink can then be examined in a broad range of frequencies [2]. Four ports fed with a normalized Gaussian pulse having a width of 3 ns are used for the purpose, Figure 3. The results obtained for each port one at a time are then combined in time by choosing appropriate time delays among them.

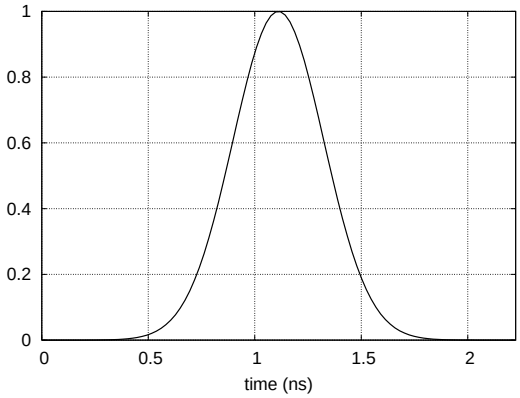

Fig. 3. Normalized Gaussian pulse.

In order to simulate the IGBT collector and the stray capacitance introduced by an insulating layer, a thin metal layer and a polyimide one are inserted in the model between each port and the heatsink, Figure 4.

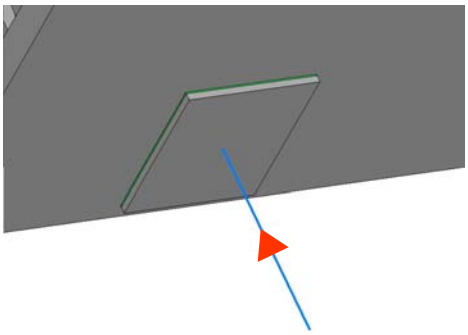

Fig. 4. Source model.

4.4 Numerical Simulations

4.4.1 Near-Field Radiation

The electric near field is analyzed in terms of the surface current density distribution on the heatsink configurations. Figures 5 and 6 show the two-dimensional plots of the maximum

values of the electric near-field magnitude reached in the time interval in which the ports 1 and 2 are excited one at a time, respectively. The plots refer to a cross-sectional view along the width at 4 cm from the sources. In the structures with two and four heatsinks, it can be noticed that the major values for the electric field are located in the gap/gaps between the excited heatsink and the adjacent unexcited one/ones. The four-heatsink configuration generates the highest emission in both simulations. Moreover, the excitation of the port 1 produces the major emission. Results for the ports 3 and 4 are not reported for symmetry reasons.

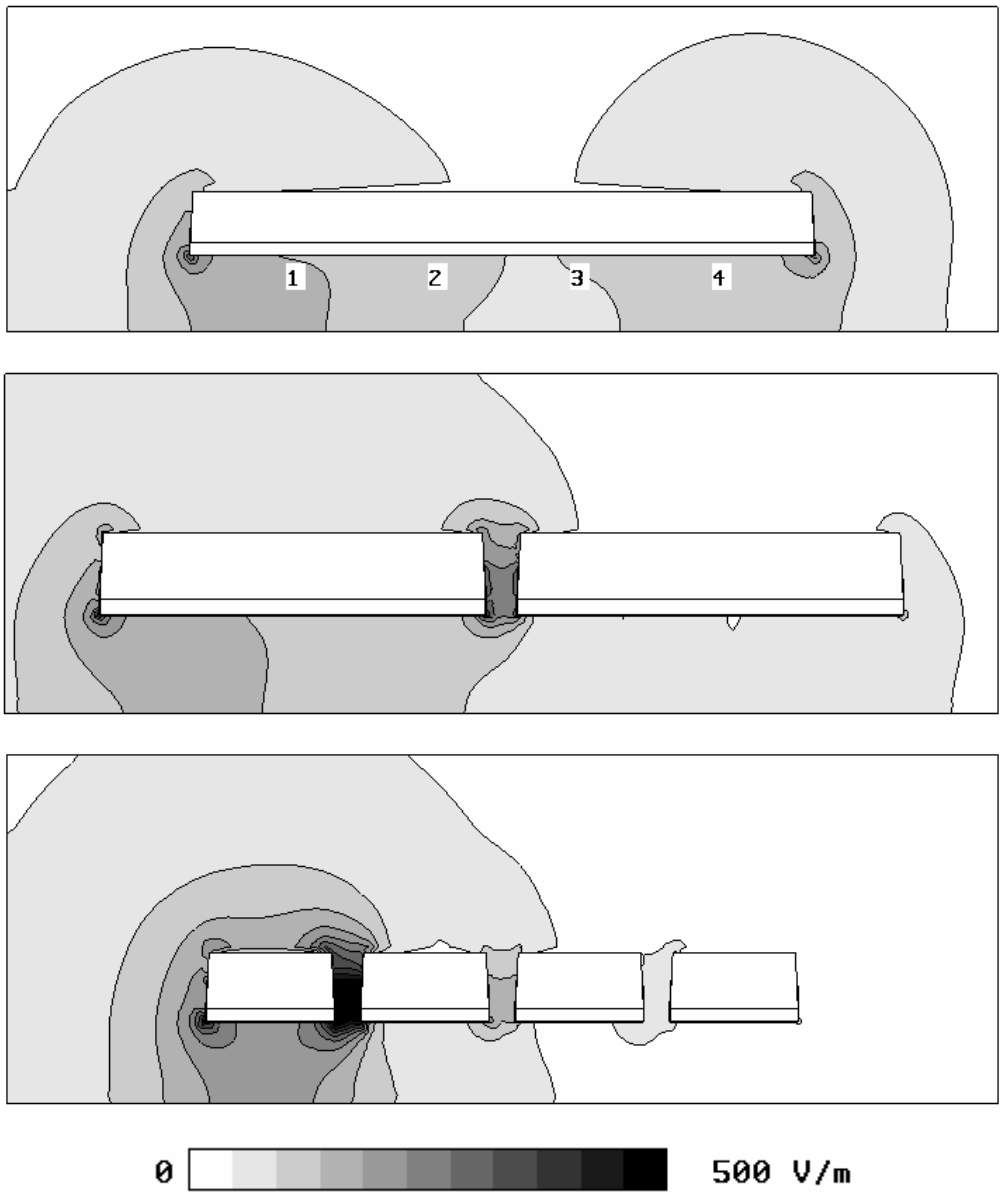

Fig. 5. Plots of the maximum values of the electric near-field magnitude during the excitation of the port 1 only, in a cross section at 4 cm from the sources.

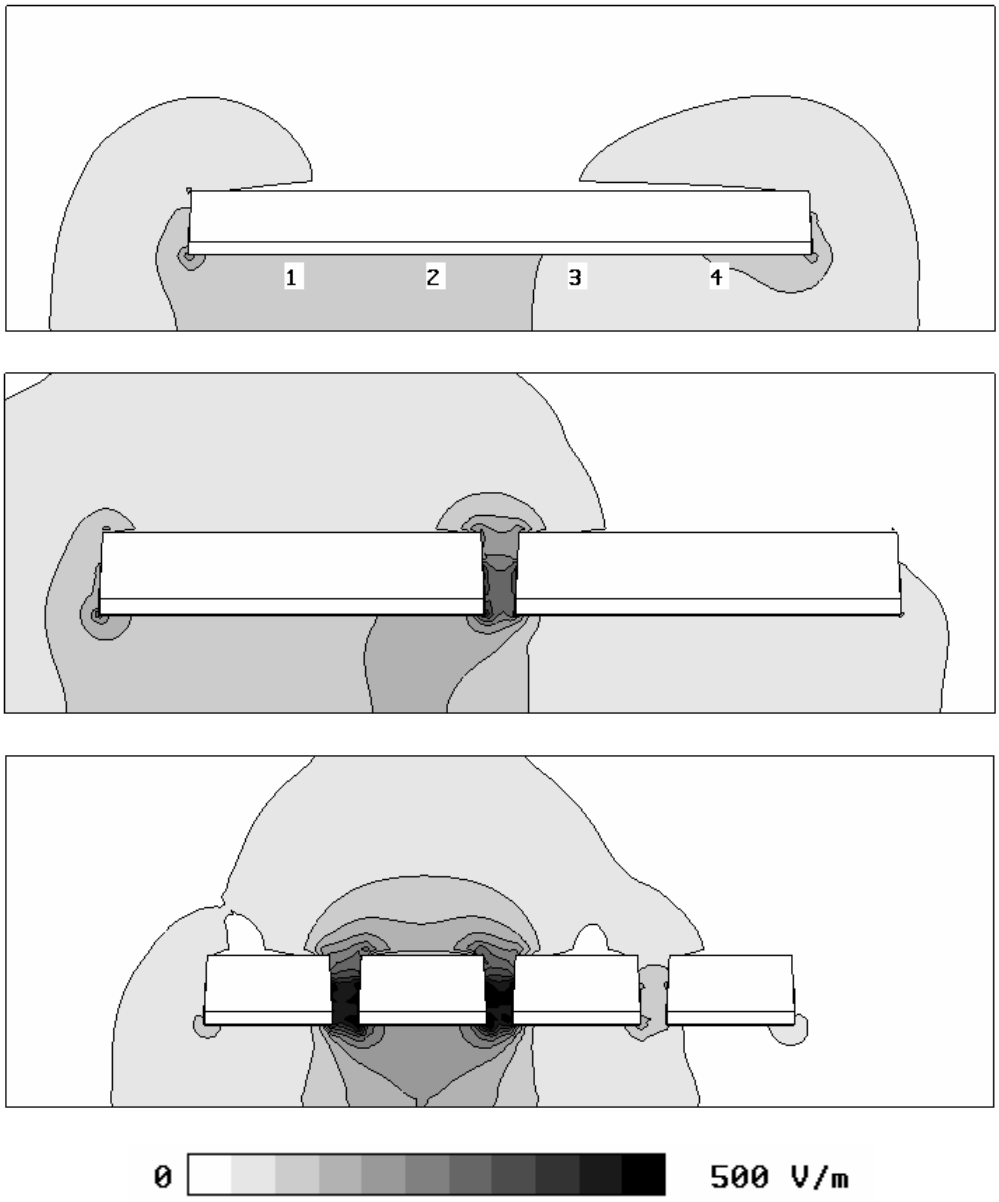

Fig. 6. Plots of the maximum values of the electric near-field magnitude during the excitation of the port 2 only, in a cross section at 4 cm from the sources.

Figures 5 and 6 show that for the one-heatsink configuration the highest values of the electric field are in the space volume between the heatsink and the ground plane, whereas for the two- and four-heatsink configurations they are between the excited heatsink and its adjacent ones. This is reasonable being the distance between two adjacent heatsinks less than that between a heatsink and the ground plane. Figure 7 depicts the two-dimensional plots of the electric near-field magnitude at an instant in which the port 2 is excited during the whole sequence of excitation.

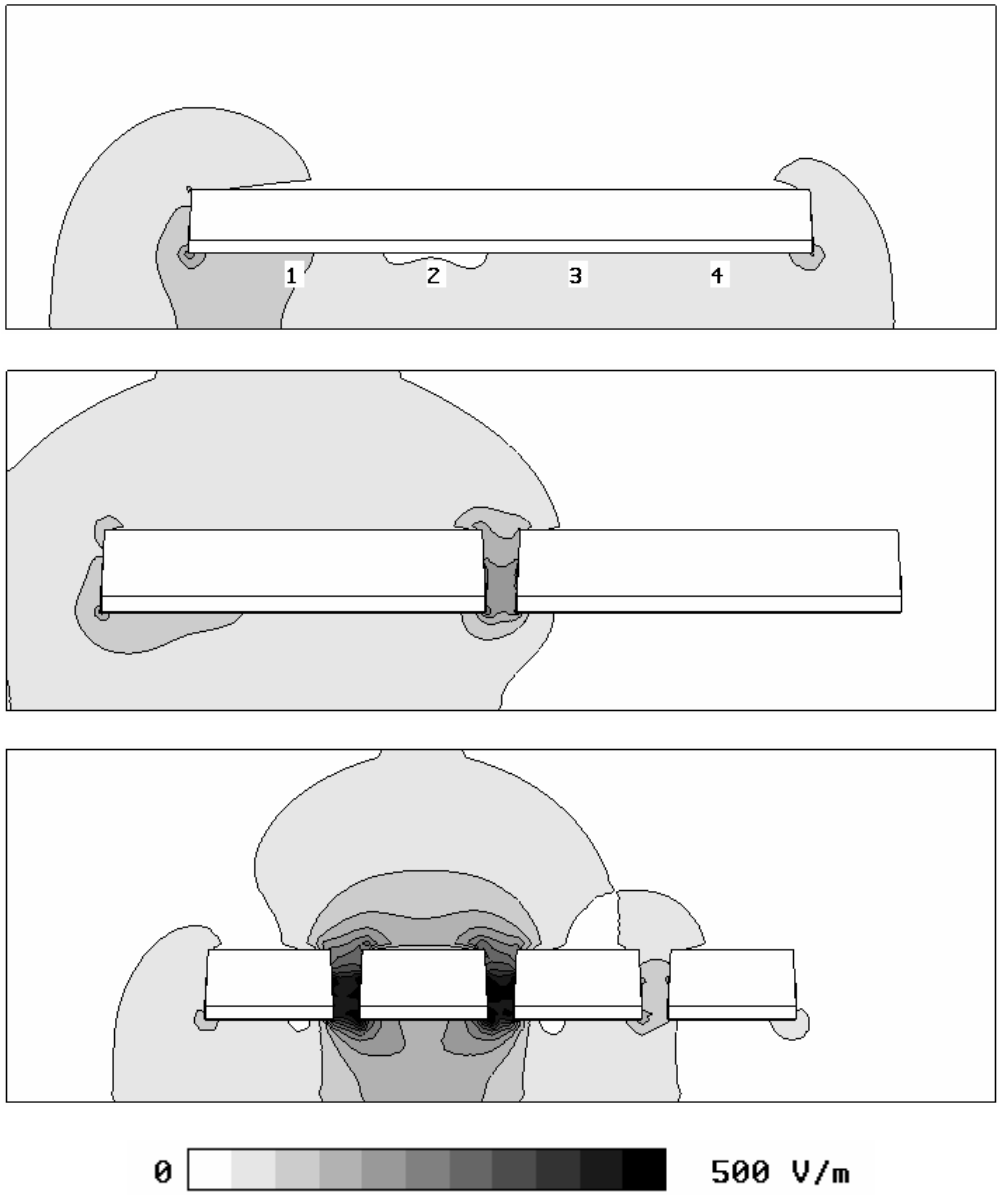

Fig. 7. Plots of the electric near-field magnitude at an instant of the excitation of the port 2 only in a cross section at 4 cm from the sources.

As in Figure 6, the highest values for the electric field are still found in the gap/gaps adjacent to the excited heatsink. In Figure 8 the surface current density distribution on the different heatsink structures generated by the excitation of the port 2 is shown. These distributions refer to the same instant of Figure 7.

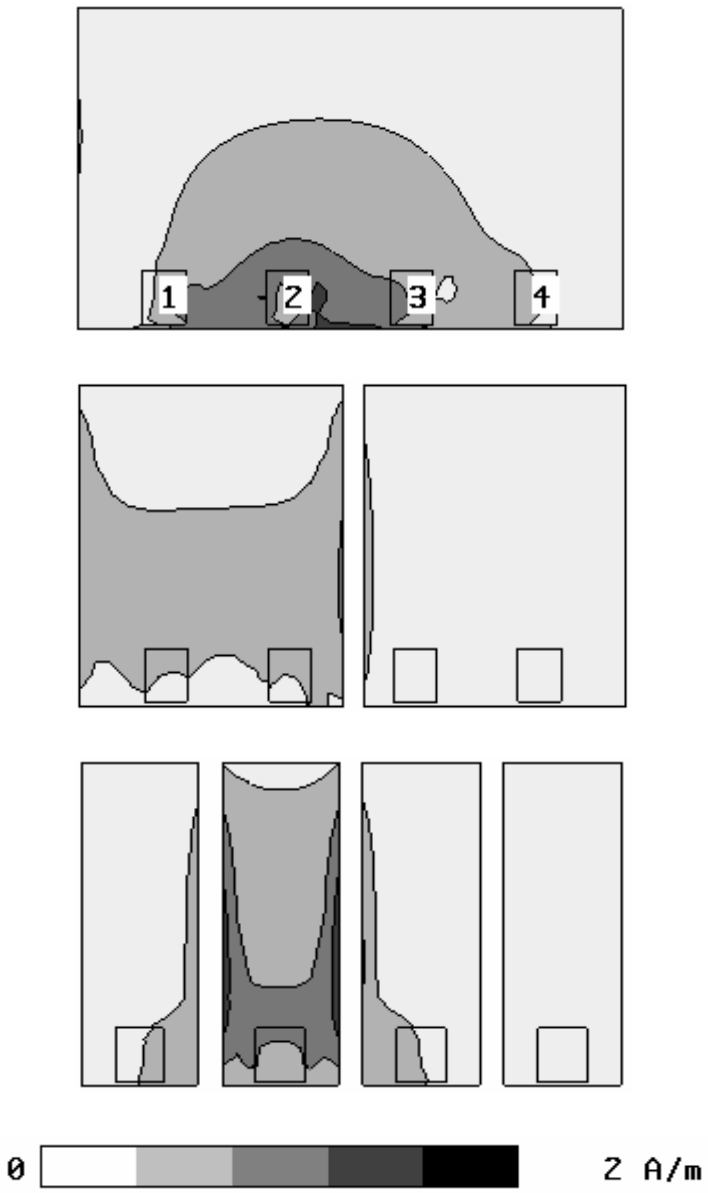

Fig. 8. Plots of the surface current density distribution at an instant of the excitation of the port 2 only in a cross section at 4 cm from the sources.

It can be noticed that in the structures with two and four heatsinks the surface current density is present in the facing boundaries between two adjacent heatsinks, one of which is excited. This phenomenon may be related to a reactive (capacitive) effect, that may be, in turn, the cause of higher electric field magnitude values in these regions. How can be noticed in Figure 9, this phenomenon interest only the lower frequencies.

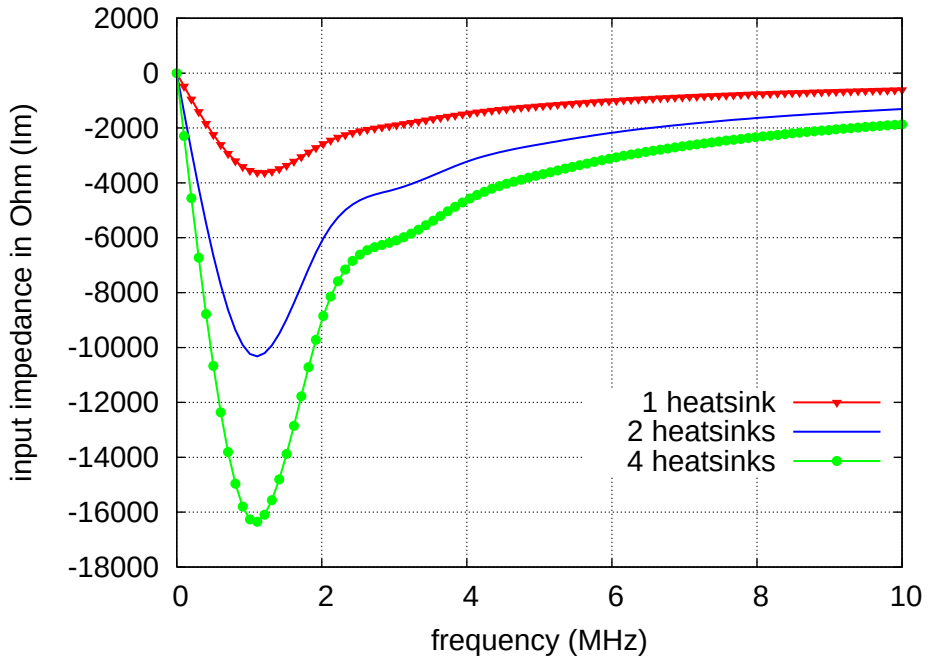

Fig. 9. Imaginary part of the input impedance in correspondence of Port 2.

The boundary of the reactive near-field region cannot be easily identified. In fact, a single heatsink can be studied as an idealized monopole or dipole antenna [2], [5]. In this case the outer boundary of the reactive near-field region is commonly taken at a distance [6]

$$R_1 = 0.62\sqrt{D^3/\lambda} \tag{1}$$

where D is the largest dimension of the antenna and λ is the wavelength at the frequency of interest. Differently, for the configurations with two and four heatsinks, it is more difficult to find the boundary of the reactive near-field region because, even if we represent each heatsink as a dipole antenna, the reactive energy flow around the heatsinks must be taken into account. Nevertheless, adopting (1), we obtain R_1 = 0.142 m for D = 250 mm and λ = 0.3 m (wavelength corresponding to 1 GHz). For the dimensions of the system and the frequency range considered, the transition between the near- and far-field regions may be taken at a distance equal to R_1.

4.4.2 Far-Field Radiation

The electric far field versus frequency is obtained transforming the time-domain waveforms into the frequency domain and the influence of the heatsink geometry and source location is considered.

According to finite-difference time-domain (FDTD) simulations of the electric far field radiated from a simplified heatsink, such as a thin rectangular sheet, there are two main dimensions to be excited, giving two main resonant frequencies. The addition of fins in the heatsink can reduce the resonant frequencies, whereas the value of the electric far-field radiation can be increased if they run parallel to the width of the sheet instead of the length [2].

To highlight the effects on the resonant frequencies of the heatsink width and the fins, simplified heatsinks, consisting of rectangular metal sheets, are considered first. In Figure 10 the electric far-field magnitude at a distance of 1 m versus frequency radiated by three sheets of 5 mm of thickness and 150 mm of length is depicted. Two sheets have a width of 20 mm and 55 mm, respectively, and one of 55 mm and fins on it. Each simplified heatsink is excited with the same source as the original one, located in a central position close to the narrowest edge of the heatsink. It can be noticed that in the 20 mm width sheet, the main resonant frequencies correspond to a wavelength double and quadruple of the longest dimension (i.e., the length): they are about 1 GHz and 500 MHz, respectively. The former resonance plays the major role. Increasing the width of the sheet and adding fins decreases the resonant frequencies.

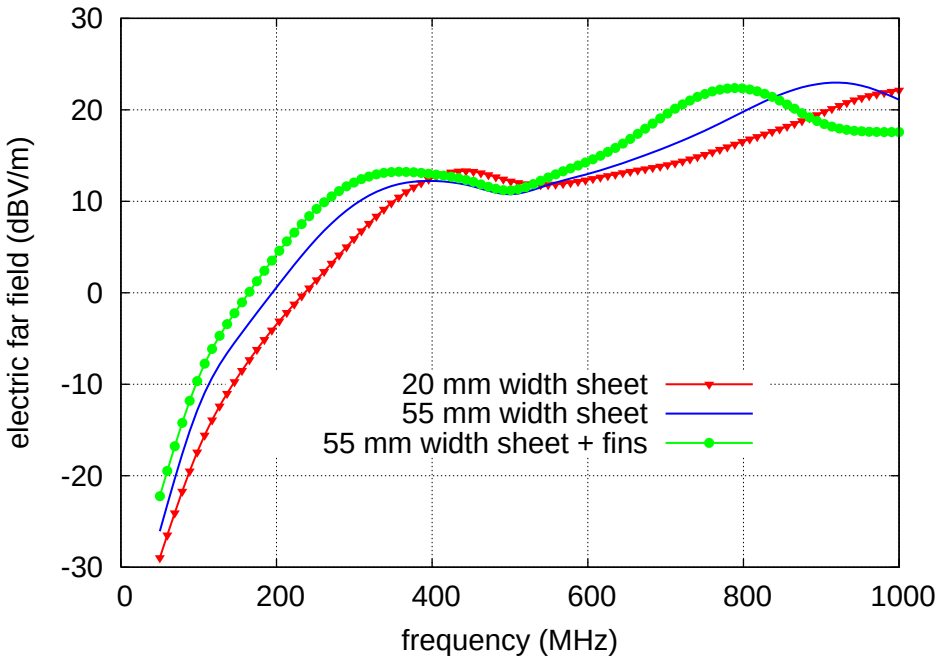

Fig. 10. Electric far-field magnitude at a distance of 1 m versus frequency for a simplified heatsink

These resonances are still visible in Figure 11, which shows the electric far-field magnitude at a distance of 1 m versus frequency for all the heatsink configurations examined exciting the port 1 only (a) and port 2 only (b), respectively. The correspondence with Figure 10 is more marked for the four-heatsink configuration, as in this case each heatsink has dimensions closer to those of the simplified heatsink. Differences between the two- and four-heatsink configurations are not particularly significant in the whole frequency range. Differently, the position of the excitation port affects the electric field radiated by the single heatsink. As it can be noticed in Figure 11, locating the excitation source close to a corner of the heatsink yields to a higher radiated electric field at about 550 MHz, that is a frequency close to the resonant frequency corresponding to a wavelength double of the heatsink width.

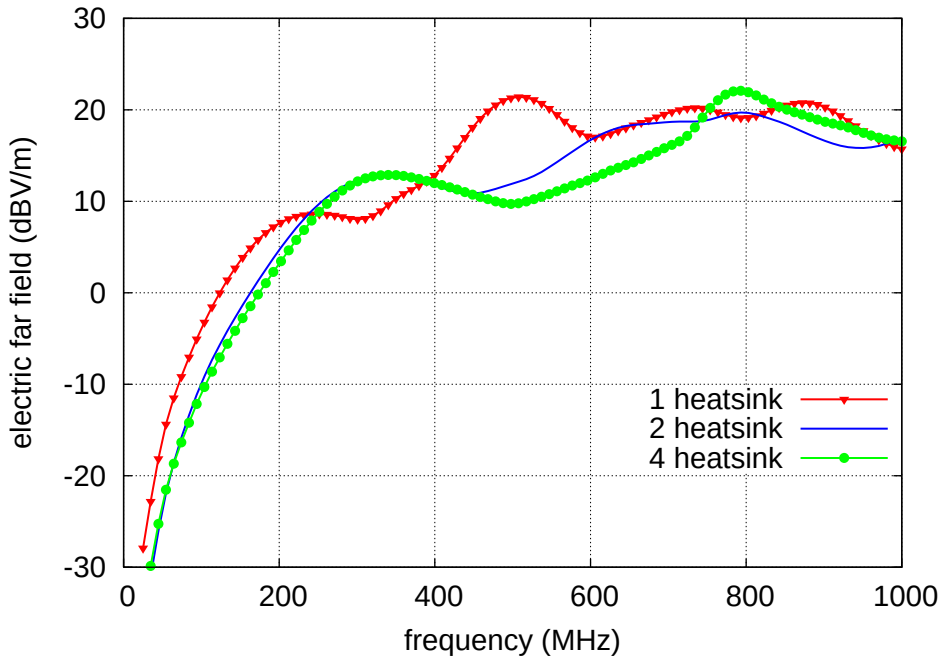

(a)

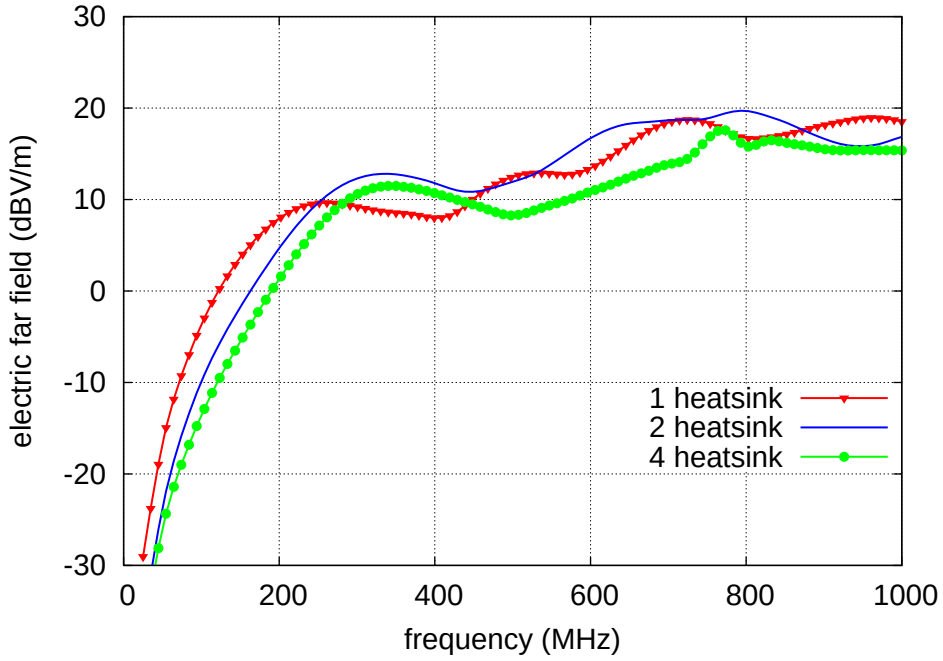

(b)

Fig. 11. Electric far-field magnitude at a distance of 1 m versus frequency. Excitation of port 1 only (a) and port 2 only (b)

The influence of the source position on the electric field radiated by the single heatsink can be investigated by studying the electromagnetic field within the air substrate between the heatsink and the ground plane. The electromagnetic field within the air substrate can be found by treating that region as a cavity bounded by perfect electric conductors at the top and

bottom surfaces (tangential electric fields vanish along these two surfaces) and by perfect magnetic walls along the perimeter of the heatsink (tangential magnetic fields vanish along those four walls), [6]. When the height h of the substrate is very small ($h << \lambda$ where λ is the wavelength within the air substrate), the field along the height can be considered constant. In addition, the fringing of the fields along the edges of the heatsink is also very small and the electric field is nearly normal to the bottom surface of the heatsink. Therefore only TM field configurations can be considered within the cavity. The field configurations within the cavity can be found using the vector potential approach described in [6]. Resonances due to the geometrical dimensions of the cavity are expected at the following frequencies:

$$(f_r)_{mnp} = \frac{c}{2\pi}\sqrt{\left(\frac{m\pi}{W}\right)^2 + \left(\frac{n\pi}{L}\right)^2 + \left(\frac{p\pi}{h}\right)^2} \qquad (2)$$

where c is the speed of light and m, n, p represent the number of half-cycle field variations along the x, y, z directions, respectively. The numerical simulations are used to validate the theoretical values from (2). A simplified single heatsink, consisting of a rectangular metal sheet, is considered first, Figure 12. The stimulation port is located alternatively in the positions a, b and c.

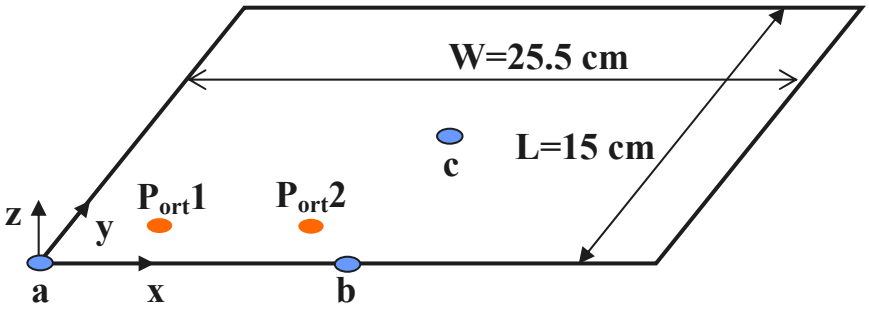

Fig. 12. Bottom surface of the heatsink and source positions.

The mode with the lowest resonance frequency is generally the dominant mode. If $W > L >> h$, the dominant mode is the TM_{100} whose resonant frequency is given by

$$(f_r)_{100} = \frac{c}{2W} \tag{3}$$

Since in our case is also $W > L > W/2 > h$ the second order mode is the TM_{010}, whose resonant frequency is given by

$$(f_r)_{010} = \frac{c}{2L} \tag{4}$$

The resonant frequencies for the first five modes are listed in Table 1. Because the small value of h the mode number p is always zero at low frequency and it's not mentioned in the Table 1.

Table 1. Resonant frequencies in MHz - Input Impedance (real part) in Ω

m	n	$f_{r,theo}$	$f_{r1,num}$	$f_{r2,num}$	$f_{r3,num}$	a (0/0)	b (12.5/0)	c (12.5/7.5)
1	0	588	588	580	510	271	–	–
0	1	1000	985	940	710	118	122	–
1	1	1160	1130	1105	895	293	–	–
2	0	1176	1155	1135	980	293	141	121
2	1	1544	1520	1485	1260	240	–	–

Columns 1 and 2 indicate the mode numbers for the first five resonant frequencies. Column 3 lists the theoretical values of the resonant frequencies calculated by formula (2) for a cavity of dimensions 255x150x1 mm. Column 4 shows the resonant frequencies obtained from the numerical simulation for a conducting plane of dimensions 255x150x1 mm located 1 mm over an infinite parallel ground plane. Columns 5 and 6 show the resonant frequencies obtained from the numerical simulation for the single heatsink located 1 mm and 30 mm over an infinite parallel ground plane, respectively. Columns 7, 8 and 9 lists the values of the real part of the input impedance computed at the stimulation port terminals, for each source position, in the proximity of the resonant frequencies (− indicates that this mode is not excited).

Figures 13 shows the simulated electric far-field magnitude at a distance of 1 m versus frequency, for a conducting plane located 1 mm over an infinite parallel ground plane, for three different source positions.

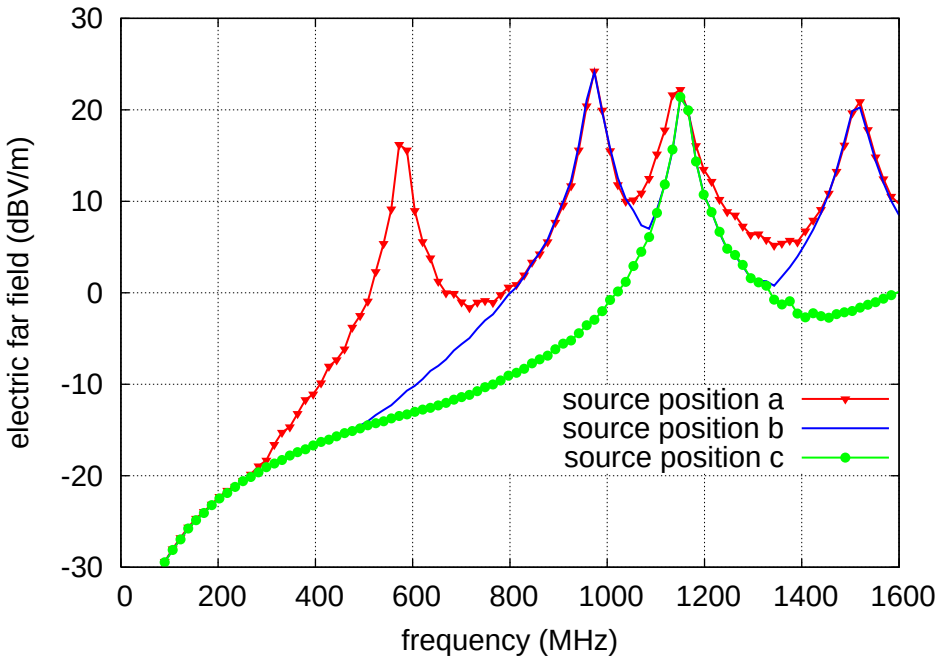

Fig. 13. Electric far-field magnitude at a distance of 1 m versus frequency for a conducting plane located 1 mm over an infinite parallel ground plane.

Figures 14 and 15 show, respectively, the electric far-field magnitude at a distance of 1 m versus frequency for the single heatsink located 1 mm and 30 mm, respectively, for three different source positions.

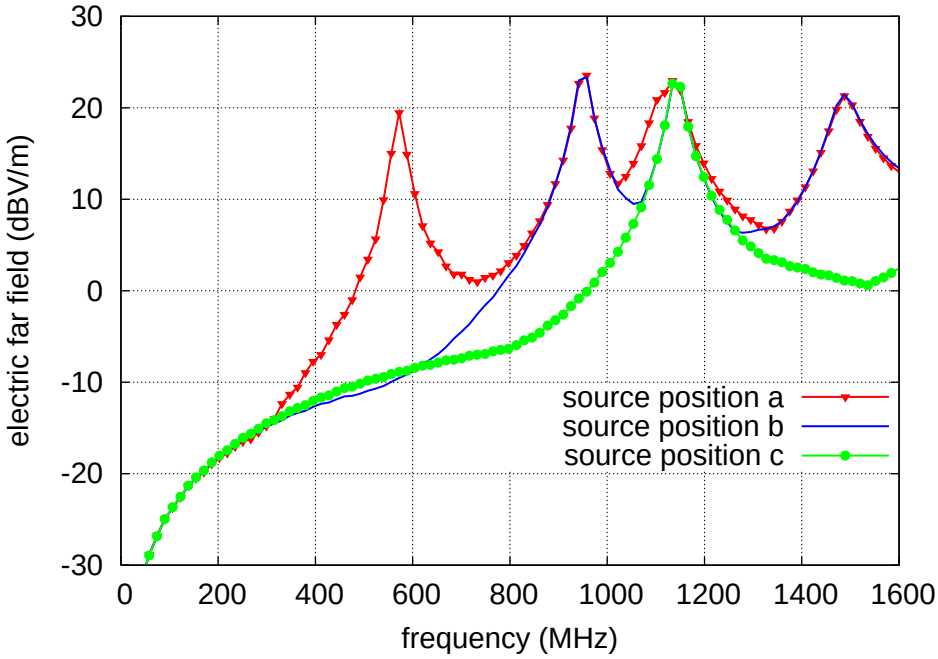

Fig. 14. Electric far-field magnitude at a distance of 1 m versus frequency for the single heatsink located 1 mm over an infinite parallel ground plane.

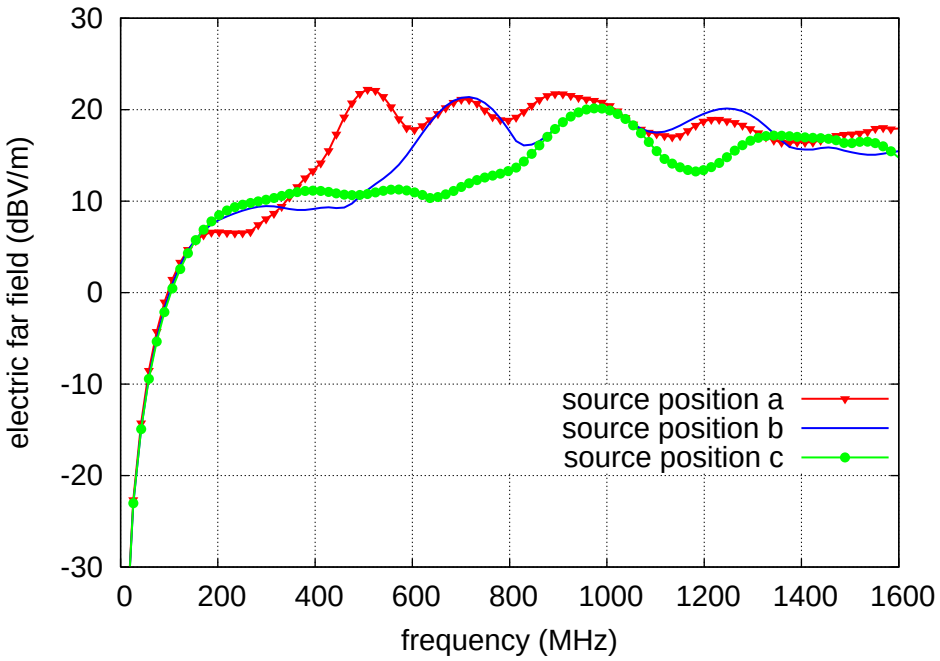

Fig. 15. Electric far-field magnitude at a distance of 1 m versus frequency for the single heatsink located 30 mm over an infinite parallel ground plane.

How can be noticed from Table 1 and Figures 13, 14, 15 not all of the modes are excited for each source point location. This behaviour can be explained when the dominating current distributions that are associated with these modes are considered. Figure 16 shows the dominant currents directions for the first four modes of the plane. If a voltage or current source is located at the centre of such a current arrow related to a particular mode it can not support this natural current flow.

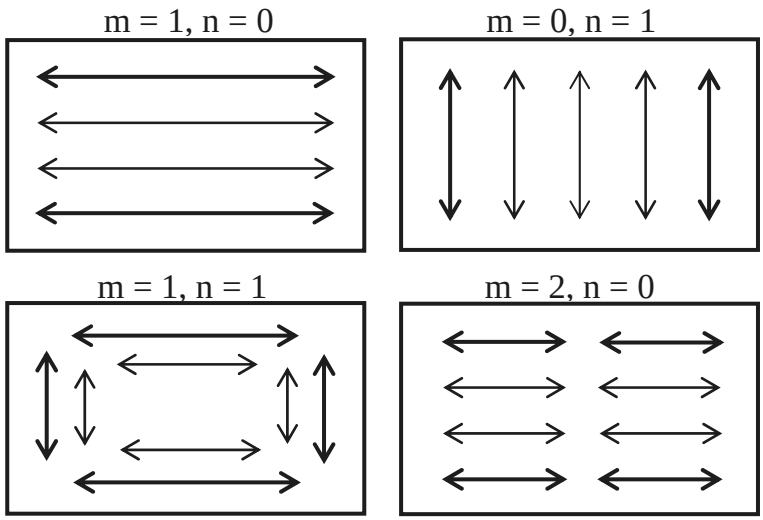

Fig. 16. Dominant current directions for mn = 10 / 01 / 11 / 20 modes

The theoretical values of the resonance frequencies are in good agreement with the numerical simulation of the conducting plane and of the heatsink when they are located 1 mm over the ground plane. At higher distances the edge effect generates a bending of the electric field line respect the normal direction of the substrate. This bending can be taken in account by assigning at the heatsink higher dimensions respect the real dimensions, or by multiplying (2) for the following coefficient:

$$q = \frac{f_{r,num}}{f_{r,theo}} \tag{5}$$

To have a first indication at which frequencies maximum values for the field strength must be expected, the radiated power from the structures can be calculated as:

$$P_{rad} = \frac{1}{2} \cdot R_{rad} \cdot |I|^2 \tag{6}$$

where R_{rad} is the radiation resistance and I is the amplitude of the injected current. The real part of the input impedance of a lossless antenna represents his radiation resistance. The power dissipated as heat on the internal resistance of the source and the heat dissipated by the heatsink is not considered in this study. In the case of the discrete source of Figure 2 the injected current is given by

$$I = \frac{Z_s}{Z_{input} + Z_s} \cdot I_s \tag{7}$$

Figures 17 shows the electric far-field magnitude at a distance of 1 m versus frequency, for a conducting plane located 1 mm over an infinite parallel ground plane and over a finite ground plane of the same dimensions of the heatsink area.

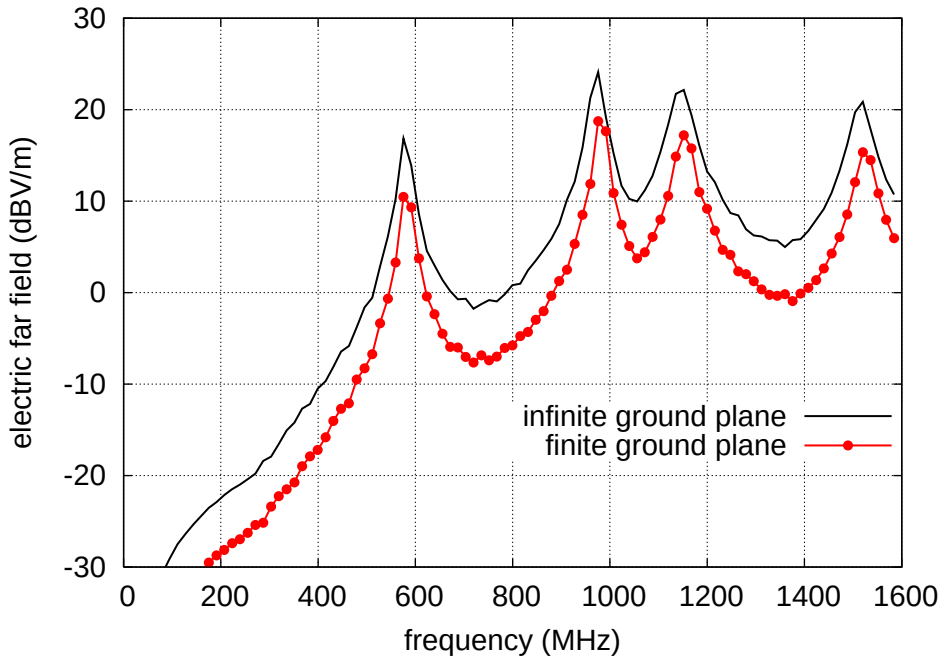

Fig. 17. Electric far-field magnitude at a distance of 1 m versus frequency for a plane located 1 mm over an infinite and a finite, parallel ground plane.

With an infinite parallel ground plane all the radiated power is forced to spread all over the structure and hence, the electric far field radiated is maximum. The finite ground plane is useful to study different layouts of the structure composed by the heatsink and the PCB. The plane is used instead of the heatsink to reduce the simulation time. The effect of the addition of the fins has been already investigated in Figures 10, 13 and 14. In Figure 18, three different layouts are shown. To highlight the influence of the structure layout on the electric far-field radiated, the worst source location, position a, has been chosen.

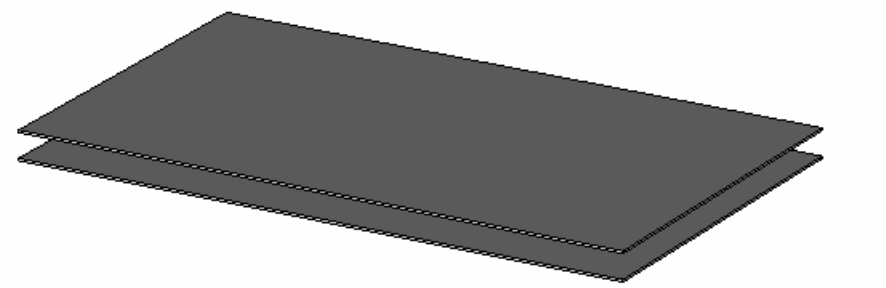

(layout 1)

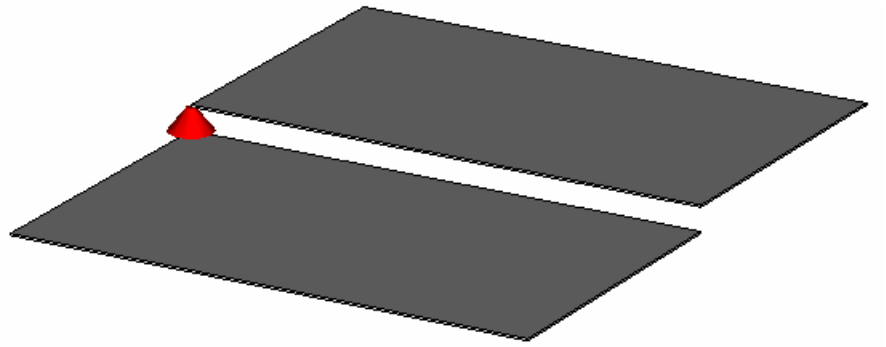

(layout 2)

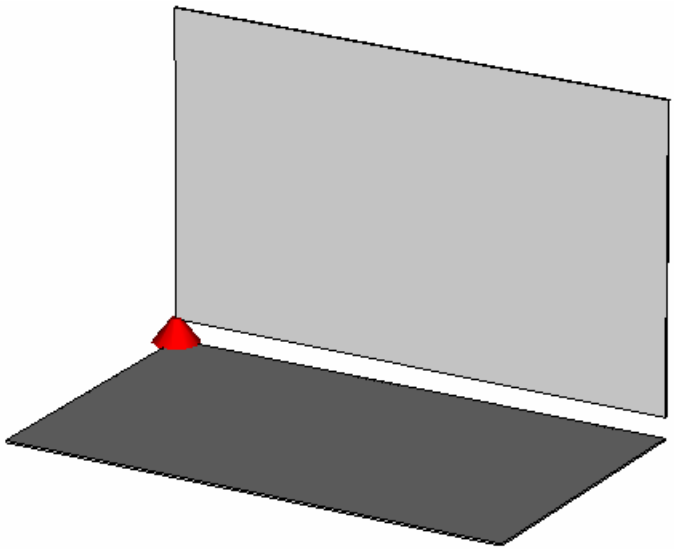

(layout 3)

Fig. 18. Three layouts examined of the structure composed by the heatsink and the PCB.

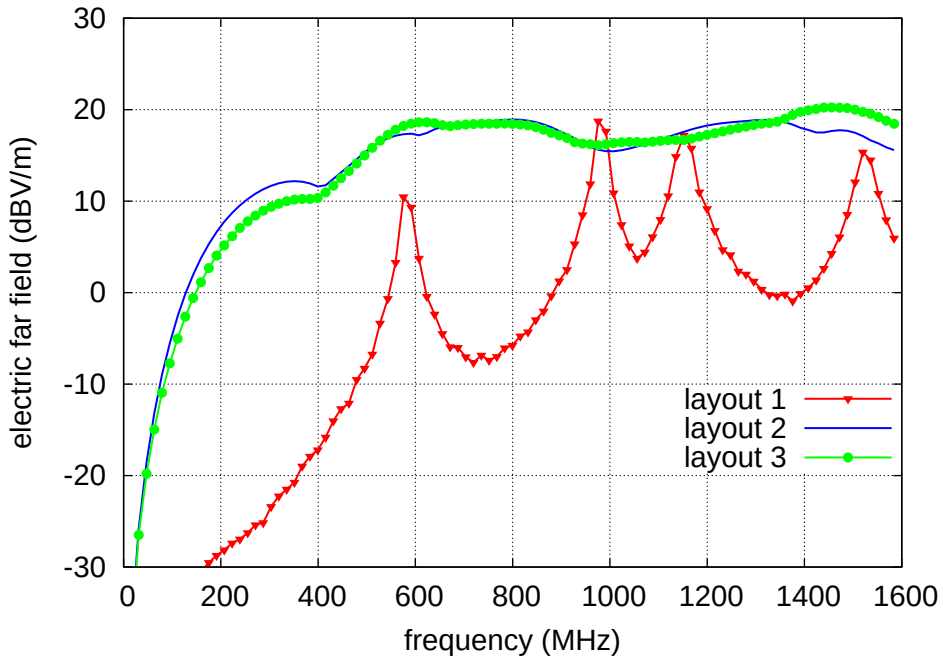

Fig. 19. Electric far-field magnitude at a distance of 1 m versus frequency for the structure layouts of Figure 18.

How can be noticed, the best way to reduce the electric far field radiated by the heatsink is to locate the electronic devices centrally on his plane area, keeping the heatsink parallel and as near as possible at the PCB.

4.5 Summary

In this chapter the radiated emissions from structures with one, two and four heatsinks are analyzed by means of numerical simulations. Results show that, at a generic instant of the excitation source, in the two- and four-heatsink configurations the highest values for the electric near field are located in the gap/gaps between two adjacent heatsinks, one of which is excited. This phenomenon may be related to a reactive (capacitive) effect. The surface current density distributes on the heatsink accordingly. The far field is examined transforming the electric field time waveform into the frequency domain. In the two- and four-heatsink structures, the location of the excitation source does not affect the radiated electric far field significantly, whereas for the single heatsink an increase of the electric field is noticed when the source is located close to a corner of the structure. The theory of the cavities is used to understand and to verify the resonance frequencies of the structures in far field, and to relate

them with the source position and the geometrical dimensions of the heatsink. Finally, the influence of the position of the heatsink with respect to the PCB is studied in terms of the electric far-field emission.

The results in this chapter were published by the author in [7].

References

[1] M. Mardiguian, *Controlling radiated emissions by design*, 2nd edition, Kluwer Academic Publishers, Massachusetts, USA, 2001.

[2] N. J. Ryan, B. Chambers and D. A. Stone, "FDTD modeling of heatsink RF characteristics for EMC mitigation", *IEEE Transactions on Electromagnetic Compatibility*, Vol. 44, August, 2002, pp. 458-465.

[3] A. E. Ruehli and H. Heeb, "Circuit models for three-dimensional geometries including dielectrics", *IEEE transactions on Antennas and Propagation*, Vol. 40, July 1992, pp. 1507-1516.

[4] T. Weiland, "A discretization method for the solution of Maxwell's equations for six components fields", *Electronics and Communication*, (AEU), Vol. 31, 1977, pp. 116–120.

[5] S. K. Das and T. Roy, "An investigation on radiated emissions from heatsinks", in *Proc. IEEE International Symposium on Electromagnetic Compatibility*, Denver, August, 1998, pp. 784-789.

[6] C. A. Balanis, *Antenna theory: analysis and design*, 2nd edition, J. Wiley & Sons, Inc., New York, USA, 1997.

[7] A. Dolente, U. Reggiani and L. Sandrolini, "Comparison of radiated emissions from different heatsink configurations", *VI International Symposium on Electromagnetic Compatibility and Electromagnetic Ecology*, St. Petersburg, Russia, June 2005.

CHAPTER 5

“Conclusions and Open Problems”

5.1 Conclusions

The influence of different heatsink configurations for SMPS on conducted EMI and on its CM and DM components is considered in the first part of the third chapter. It is emphasized the effect of the stray capacitances introduced by three different heatsink configurations through conducted EMI measurements. The advantage of reduction of the stray capacitance to ground is lost in the grounded configuration due to the not negligible inductance of the connection to ground.

The main frequencies of noise in the CM conducted emission spectrum can be reduced by subdividing the heatsink among the switching devices of the main commutation loop, and by using a common-mode choke on the connection to ground of just one heatsink leaving each other heatsink ungrounded. This new filtering technique is verified by experimental results.

In order to limit the CM currents at the design level of the SMPS, it’s necessary to limit the overvoltages at the transistor terminals caused by the switching operations. To predict these overvoltages, a modeling technique that focuses on the high frequency equivalent circuit of the power supply is proposed. The simulation of complex topologies in power electronics requires the prediction of electromagnetic coupling effects. Therefore, distributed models of stray inductance for coplanar strip and coplanar waveguide topology of the switching circuit are also investigated using the FDTD and HFSS based simulations. The described and proposed modeling technique is verified by the measurements and PSPICE simulations. Overall, the results validate the use of high frequency equivalent circuit and lumped inductance models for the design of power electronic circuits.

In the forth chapter, the radiated emissions from structures with one, two and four heatsinks are analyzed by means of numerical simulations. Results show that, at a generic instant of the excitation source, in the two- and four-heatsink configurations the highest values for the

electric near field are located in the gap/gaps between two adjacent heatsinks, one of which is excited. This phenomenon may be related to a reactive (capacitive) effect. The far field is examined transforming the electric field time waveform into the frequency domain. The theory of the cavities is used to understand and to verify the resonance frequencies of the structures in the far field, and to relate them with the source position and the geometrical dimensions of the heatsink. Finally, the influence of the position of the heatsink with respect to the PCB is studied in terms of the electric far field emission.

5.2 Open Problems

The distributed inductance models introduced to study the voltage applied at the heatsink are limited to specific topologies and do not take into account the real return current path that contributes to the interconnection inductance. The work on the extraction of compact inductance models from the numerical simulations is an open problem for future analysis.

With regard to the radiated emission from the heatsinks, more research is needed to understand the interactions among the heatsink and others components of the SMPS such as the booster transformer and the external interconnections of the PCB.